

# Stellar contents and star formation in the young star cluster Be 59

A. K. Pandey,<sup>1,2,3\*</sup> Saurabh Sharma,<sup>3</sup> K. Ogura,<sup>4</sup> D. K. Ojha,<sup>2</sup> W. P. Chen,<sup>1</sup>  
B. C. Bhatt<sup>5</sup> and S. K. Ghosh<sup>2</sup>

<sup>1</sup>*Institute of Astronomy, National Central University, Chung-Li 32054, Taiwan*

<sup>2</sup>*Tata Institute of Fundamental Research, Mumbai 400 005, India*

<sup>3</sup>*Aryabhata Research Institute of Observational Sciences (ARIES), Manora Peak, Nainital 263 129, India*

<sup>4</sup>*Kokugakuin University, Higashi, Shibuya-ku, Tokyo 150-8440, Japan*

<sup>5</sup>*CREST, Indian Institute of Astrophysics, Hosakote 562 114, India*

Accepted 2007 October 24. Received 2007 October 14; in original form 2007 August 8

## ABSTRACT

We present  $UBVI_c$  CCD photometry of the young open cluster Be 59 with the aim to study the star formation scenario in the cluster. The radial extent of the cluster is found to be  $\sim 10$  arcmin (2.9 pc). The interstellar extinction in the cluster region varies between  $E(B - V) \simeq 1.4$  to 1.8 mag. The ratio of total-to-selective extinction in the cluster region is estimated as  $3.7 \pm 0.3$ . The distance of the cluster is found to be  $1.00 \pm 0.05$  kpc. Using near-infrared (NIR) colours and slitless spectroscopy, we have identified young stellar objects (YSOs) in the open cluster Be 59 region. The ages of these YSOs range between  $< 1$  and  $\sim 2$  Myr, whereas the mean age of the massive stars in the cluster region is found to be  $\sim 2$  Myr. There is evidence for second-generation star formation outside the boundary of the cluster, which may be triggered by massive stars in the cluster. The slope of the initial mass function,  $\Gamma$ , in the mass range  $2.5 < M/M_\odot \leq 28$  is found to be  $-1.01 \pm 0.11$  which is shallower than the Salpeter value ( $-1.35$ ), whereas in the mass range  $1.5 < M/M_\odot \leq 2.5$  the slope is almost flat. The slope of the  $K$ -band luminosity function is estimated as  $0.27 \pm 0.02$ , which is smaller than the average value ( $\sim 0.4$ ) reported for young embedded clusters. Approximately 32 per cent of  $H\alpha$  emission stars of Be 59 exhibit NIR excess indicating that inner discs of the T Tauri star (TTS) population have not dissipated. The Midcourse Space Experiment (MSX) and *IRAS-HIRES* images around the cluster region are also used to study the emission from unidentified infrared bands and to estimate the spatial distribution of optical depth of warm and cold interstellar dust.

**Key words:** open clusters and associations: individual: Be 59 – stars: formation – stars: luminosity function, mass function – stars: pre-main-sequence.

## 1 INTRODUCTION

High-mass star-forming regions have been known for many years as OB associations and H II regions, and they have been observed quite extensively on various aspects. However, the census of low-mass stars in such regions has not been possible until recently. Recent advancement in detectors has permitted the detection of substantial population of low-mass stars in OB associations. Recently, relatively large number of low-mass stars have been detected in a few OB associations (e.g. Upper Scorpius, the  $\sigma$  and  $\lambda$  Ori regions; Preibisch & Zinnecker 1999; Dolan & Mathieu 2002). Since this realization, surveys have demonstrated that the initial mass functions (IMFs) are essentially the same in all star-forming regions. The apparent difference may be mainly due to the inherent low percentage of high-mass stars and the incomplete survey of low-mass stars in high-

mass star-forming regions (e.g. Massey, Johnson & Eastwood 1995; Hillenbrand 1997; Preibisch & Zinnecker 1999; Kroupa 2002).

The massive stars of OB associations have strong influence and significantly affect the entire star-forming region. Strong ultraviolet (UV) radiation from massive stars could evaporate nearby clouds and consequently terminate star formation. Herbig (1962) suggested that low- and intermediate-mass stars form first, and with the formation of most massive star in the region, the cloud gets disrupted and star formation ceases. Alternatively, shock waves associated with the ionization front (IF) may squeeze molecular cloud and induce subsequent star formation. Elmegreen & Lada (1977) proposed the expanding IFs play a constructive role to incite a sequence of star formation activities in the neighbourhood. The question, however, is: could both of these effects occur in different parts of the same star-forming regions?

Recent studies have shown cases where massive stars ionize adjacent clouds revealing embedded stars (e.g. the Eagle Nebula; Hester et al. 1996). Preibisch & Zinnecker (1999) show that star formation

\*E-mail: pandey@aries.ernet.in

**Table 1.** Log of observation.

Telescope/date	Filter	Exp. (s) × No. of frames
Kiso Schmidt, Japan		
2001 November 19	<i>U</i>	180 × 15
”	<i>B</i>	180 × 10, 60 × 16, 10 × 6
”	<i>V</i>	60 × 16, 10 × 9
2001 November 20	<i>I<sub>c</sub></i>	60 × 3, 10 × 10
<i>HCT</i> , IIA		
2004 September 22, and 2005 January 7, 8, 9	H $\alpha$ with grism in	(420 × 3) × 9 positions
”	H $\alpha$ without grism	(60 × 3) × 9 positions

in the upper Scorpius OB association was likely triggered by a nearby supernovae. Recently, Lee et al. (2005) have found evidence for triggered star formation in the bright-rimmed clouds (BRCs) in the vicinity of O stars. Pandey et al. (2001, 2005) found that star formation in a few young clusters may be a continuous process. For example, in the case of NGC 663, star formation seems to have taken place non-coevally in the sense that formation of low-mass stars precedes the formation of most massive stars. Whereas, in the case of NGC 654 and 3603, formation of low-mass stars did not cease after the formation of most massive stars in the clusters.

The sharpless region S171 is a large H II region associated with the Cepheus OB4 stellar association (Yang & Fukui 1992). The star cluster Be 59 is located at the centre of the nebulous region with nine O7-B3 stars. The physical properties of the ionized gas have been investigated in radio continuum and recombination lines (e.g. Felli et al. 1977; Rossano, Russell & Cornett 1980; Harten et al. 1981). Yang & Fukui (1992) have mapped the molecular gas distribution using the  $J = 1 - 0$  lines of  $^{12}\text{CO}$  and  $^{13}\text{CO}$  emission, indicating that Be 59 generates the IF on the surface of two dense molecular clouds. They suggested that the dense gas is in contact with the continuum source, and IF is deriving shocks into the clumps. As the shock penetrates into the molecular clumps, it forms a compressed gas layer which is unstable against self-gravity (Elmegreen 1989, 1998). One can expect that a new generation of stars may form from the compressed gas layer. Thus, the S171 region provides an opportunity to make a comprehensive exploration of the effects of massive stars on low-mass star formation. Therefore, in this paper, we present a multiwavelength study of the star-forming region S171. We have also carried out slitless spectroscopy to identify pre-main-sequence H $\alpha$  emission stars in the region. In Section 2, we present optical CCD photometric and slitless spectroscopic observations and a brief description of data reduction. In Section 3, we discuss archival data set used in the present study. In the ensuing sections, we discuss results and star formation scenario in the Be 59 region.

## 2 OBSERVATIONS AND DATA REDUCTION

### 2.1 *UBVI<sub>c</sub>* CCD observations

The CCD *UBVI<sub>c</sub>* observations of the cluster were obtained using the 105-cm Schmidt telescope of the Kiso Observatory on 2001 November 19–21. The CCD camera used a SITe 2048 × 2048 TK2048E chip having a pixel size of 24  $\mu\text{m}$ . At the Schmidt focus ( $f/3.1$ ), each pixel corresponds to 1.5 arcsec, and the entire chip covers a field of  $\sim 50 \times 50$  arcmin<sup>2</sup> on the sky. The read-out noise and gain of the CCD are 23.2  $e^-$  and 3.4  $e^-/\text{ADU}$ , respectively. A number of short and deep exposure frames were taken. The log of the observations is given in Table 1. A number of bias and dome flat frames

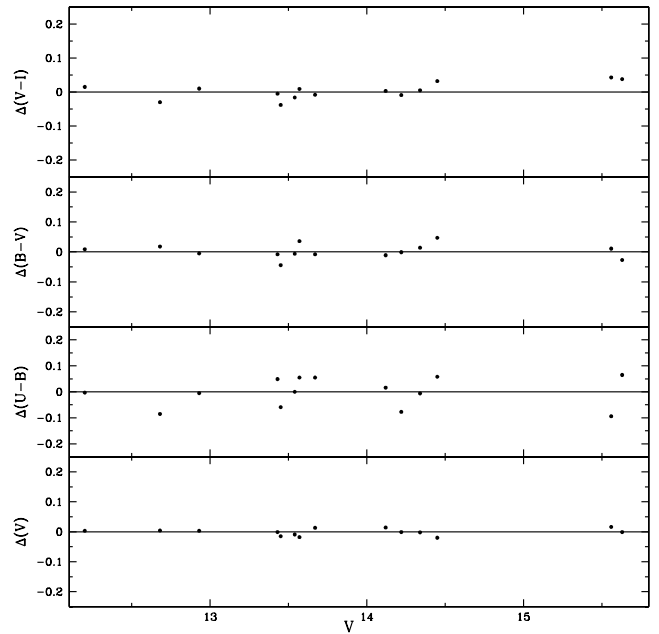


**Figure 1.** Residuals between standard and transformed magnitudes and colour of standard stars plotted against standard *V* magnitude.

were also taken during the observing runs. The observations were standardized by observing 14 standard stars in SA95 field (Landolt 1992) with brightness  $12.2 < V < 15.6$  and colour  $0.45 < (B - V) < 1.51$  on 2001 November 22.

The data analysis was carried out at Aryabhata Research Institute of Observational Sciences (ARIES), Nainital. Initial processing of the data was done using IRAF<sup>1</sup> and ESO-MIDAS<sup>2</sup> data reduction software packages. The photometry was carried out by using DAOPHOT II software (Stetson 1987). The point spread function (PSF) was obtained for each frame using several uncontaminated stars. Full width at half-maximum (FWHM) of the star images was  $\sim 3$  arcsec. When bright stars were saturated on deep exposure frames, their magnitudes were taken from short exposure frames. Calibration of the instrumental to the standard system was done using the procedure outlined by Stetson (1992). The details of the procedure, zero-point constants, colour coefficients and extinction coefficients are given elsewhere (Sharma et al. 2006). Fig. 1 shows the standardization residuals,  $\Delta$ , between the standard and transformed *V* magnitudes

<sup>1</sup> IRAF is distributed by National Optical Astronomy Observatories, USA.

<sup>2</sup> ESO-MIDAS is developed and maintained by the European Southern Observatory.

**Table 2.**  $UBVI_c$  photometric data of the stars in the field of Be 59.  $X, Y$  are the pixel coordinates. Radius is with respect to the centre  $X = 1128$ ,  $Y = 1024$  ( $\alpha_{2000} = 00^{\text{h}}02^{\text{m}}10^{\text{s}}.4$ ,  $\delta_{2000} = 67^{\circ}25'10''$ ). One pixel corresponds to 1.5 arcsec. The complete table is available in electronic form only.

Star no.	$X$ (pixel)	$Y$ (pixel)	$V$ (mag)	$B - V$ (mag)	$V - I$ (mag)	$U - B$ (mag)	Radius (pixel)	$\alpha_{2000}$ (h:m:s)	$\delta_{2000}$ (d:m:s)
1	1128.92	1023.27	19.126	—	—	—	1.17	00:02:10.13	67:25:08.6
2	1117.29	1028.99	18.508	—	3.039	—	11.81	00:02:13.15	67:25:17.2
3	1115.29	1020.07	11.301	1.143	1.426	0.008	13.30	00:02:13.69	67:25:03.9
4	1134.18	1011.54	17.654	2.193	3.024	—	13.90	00:02:08.78	67:24:50.9
5	1143.74	1012.27	19.475	—	3.622	—	19.63	00:02:06.29	67:24:51.9
6	1147.39	1014.66	18.303	2.421	3.159	—	21.52	00:02:05.33	67:24:55.5
7	1137.94	1045.48	13.873	1.241	1.648	1.181	23.66	00:02:07.74	67:25:41.8
8	1146.54	1040.00	18.657	1.723	2.554	—	24.48	00:02:05.50	67:25:33.5

and  $(U - B)$ ,  $(B - V)$  and  $(V - I)$  colours of standard stars. The standard deviation in  $\Delta V$ ,  $\Delta(U - B)$ ,  $\Delta(B - V)$  and  $\Delta(V - I)$  is 0.010, 0.055, 0.023 and 0.023 mag, respectively. The photometric errors increase with  $V$  magnitude and become larger ( $\geq 0.1$  mag) for stars fainter than  $V = 19.5$  mag. The measured photometric data along with positions of all the stars are given in Table 2,<sup>3</sup> a sample of which is given in this paper.

To study the luminosity function (LF) and mass function (MF), it is very important to make necessary corrections in the data sample to take into account the incompleteness that may occur for various reasons (e.g. due to the crowding of stars). We used the ADDSTAR routine of DAOPHOT II to determine the completeness factor (CF). The procedure has been outlined in detail in our earlier work (Pandey et al. 2001, 2005). The sample is complete at the brighter magnitude level ( $V \leq 14$ ). The incompleteness increases with increasing magnitude as expected (e.g. CF  $\sim 0.84$  for  $V = 19$ ).

## 2.2 Grism slitless spectroscopy

The observations were also carried out in slitless mode with a grism as the dispersing element using the Himalayan Faint Object Spectrograph Camera (HFOSC) instrument at the 2-m *Himalayan Chandra Telescope* (HCT) on 2004 September 22 and 2005 January 7–9. This mode of observation using the HFOSC yields an image where the stellar images are replaced by their spectra. A combination of a wide  $H\alpha$  filter ( $\lambda = 6300\text{--}6740 \text{ \AA}$ ) and Grism 5 (5200–10 300  $\text{\AA}$ ) of HFOSC was used without any slit. The resolution of the grism is 870. The central  $2\text{K} \times 2\text{K}$  pixel of the  $2\text{K} \times 4\text{K}$  CCD was used for data acquisition. The pixel size is  $15 \mu\text{m}$  with the scale of  $0.297 \text{ arcsec pixel}^{-1}$ . We secured three spectroscopic frames of 7 min exposure with grism in, and three direct frames of 1 min exposure with the grism out. The seeing during the observations was  $\sim 1.5$  to  $2.3$  arcsec. The co-added spectroscopic frames yield limiting magnitude of about  $V \sim 20$  for continuum detection. The slitless spectra thus obtained were used to identify the emission line stars in the field of the cluster. The data were reduced following the procedures with IRAF as described by Ogura, Sugitami & Pickles (2002). The equivalent width (EW) has also been calculated as described by Ogura et al. (2002) and relevant information about the detected  $H\alpha$  stars in Be 59 is given in Table 3. The frequency distribution of the  $H\alpha$  EWs reveals that 23 per cent of  $H\alpha$  stars have  $\text{EW} \leq 10 \text{ \AA}$  which is significantly less than the fraction (60 per cent) reported by Herbig (1998) in the case of IC 348. The possible cause for this deficiency

is the poor detection efficiency of smaller EWs in the present survey due to seeing conditions.

## 3 ARCHIVAL DATA SETS

Near-infrared (NIR)  $JHK_s$  data for point sources around Be 59 have been obtained from the Two-Micron All-Sky Survey (2MASS) Point Source Catalogue. The 2MASS data base provides unbiased photometry in the  $J(1.25 \mu\text{m})$ ,  $H(1.65 \mu\text{m})$  and  $K_s(2.17 \mu\text{m})$  bands to a limiting magnitude of 15.8, 15.1 and 14.3, respectively, with a signal-to-noise ratio ( $S/N$ ) of 10. To improve the photometric accuracy, we use photometric quality flag (ph-qual=AAA) which gives a  $S/N \geq 10$  and photometric uncertainty of  $< 0.10$  mag.

The Midcourse Space Experiment (MSX) surveyed the Galactic plane within the range  $|b| \leq 5^\circ$  in the four mid-infrared bands between 8 and  $21 \mu\text{m}$  at a spatial resolution of  $\sim 18.3$  arcsec (Price et al. 2001). Two of these bands (A and C) with  $\lambda(\Delta\lambda)$  corresponding to  $8.28(3.36) \mu\text{m}$  and  $12.13(1.71) \mu\text{m}$  include several Unidentified Infrared emission Bands (UIBs) at 6.2, 7.7, 8.7, 11.3 and  $12.7 \mu\text{m}$ . MSX images in the four bands around the cluster region were used to study the emission from the UIBs and to estimate the spatial distribution of optical depth of the warm interstellar dust.

The data from the *IRAS* survey in the four bands (12, 25, 60 and  $100 \mu\text{m}$ ) for the region around Be 59 were *HIRES* processed (Aumann et al. 1990) to obtain high angular resolution maps. These maps have been used to study the spatial distribution of optical depth of the cold interstellar dust. The *IRAS* point sources have also been identified in the cluster region, and their details are given in Table 4.

## 4 RESULTS

### 4.1 Structure of the cluster

#### 4.1.1 Isodensity contours

Internal interaction of two-body relaxation due to encounters among member stars and external tidal forces due to the Galactic disc or giant molecular clouds can significantly influence the morphology of the clusters. However, in the case of young clusters, where dynamical relaxation is not important because of cluster's young age, the stellar distribution can be considered as the initial morphology of the cluster that should be governed by the initial conditions in the parent molecular cloud (Chen, Chen & Shu 2004). To study the morphology of the clusters, we plotted isodensity contours for the sample of main sequence (MS) (cf. Pandey et al. 2001) stars having  $V \leq 18$  mag (Fig. 2, left-hand panel). Similarly, the isodensity contours using the 2MASS data are also plotted in Fig. 2 (right-hand

<sup>3</sup> Table 2 is available in electronic form only.

**Table 3.** Detected H $\alpha$  emission stars.

ID	$\alpha_{2000}$ (h:m:s)	$\delta_{2000}$ (d:m:s)	EW ( $\text{\AA}$ )	$V$ (mag)	$B - V$ (mag)	$V - I$ (mag)
1	00:00:03.93	+67:35:55.1	15	19.218	2.121	2.794
2	00:00:08.23	+67:35:47.1	12	–	–	–
3	00:00:12.02	+67:34:42.1	76	–	–	–
4	00:00:18.68	+67:28:09.8	19	19.308	–	3.023
5	00:00:20.40	+67:27:17.0	47	–	–	–
6	00:00:53.93	+67:29:25.0	3	–	–	–
7	00:01:38.76	+67:28:00.5	–	–	–	–
8	00:01:45.77	+67:17:41.3	55	19.084	–	3.054
9	00:01:48.40	+67:27:28.5	25	18.738	2.407	3.235
10	00:01:50.02	+67:30:03.7	–	–	–	–
11	00:01:54.49	+67:30:17.6	56	–	–	–
12	00:01:54.99	+67:27:12.6	21	–	–	–
13	00:01:57.89	+67:23:18.5	13	17.552	2.372	2.840
14	00:01:58.09	+67:22:38.0	–	–	–	–
15	00:01:59.27	+67:24:34.6	16	–	–	–
16	00:02:00.39	+67:23:57.4	8	15.900	1.837	2.236
17	00:02:02.05	+67:23:05.5	11	18.667	2.367	3.349
18	00:02:02.29	+67:22:36.1	–	–	–	–
19	00:02:02.55	+67:22:38.6	–	–	–	–
20	00:02:02.56	+67:36:46.8	–	–	–	–
21	00:02:04.68	+67:36:49.1	–	–	–	–
22	00:02:06.31	+67:24:51.9	–	19.475	–	3.622
23	00:02:07.82	+67:28:38.0	11	19.528	–	3.333
24	00:02:15.08	+67:29:27.0	25	18.268	2.417	2.754
25	00:02:16.33	+67:23:37.0	19	18.991	–	3.476
26	00:02:19.64	+67:18:13.3	8	18.585	3.117	3.467
27	00:02:24.51	+67:28:20.2	8	17.519	2.530	3.132
28	00:02:37.34	+67:32:04.4	15	–	–	–
29	00:02:43.20	+67:34:56.7	14	19.249	–	3.212
30	00:02:46.47	+67:19:09.0	54	–	–	–
31	00:02:48.86	+67:29:01.7	6	18.347	2.445	3.110
32	00:02:57.61	+67:34:42.6	14	17.751	2.142	2.540
33	00:03:10.93	+67:35:21.7	6	18.007	2.472	2.997
34	00:03:14.72	+67:33:08.4	–	–	–	–
35	00:03:18.77	+67:30:59.5	–	–	–	–
36	00:03:19.48	+67:25:16.9	50	–	–	–
37	00:03:27.33	+67:37:56.9	14	18.676	2.350	3.031
38	00:03:28.36	+67:25:53.3	11	17.742	2.558	3.055
39	00:03:35.14	+67:38:25.4	–	–	–	–
40	00:03:49.93	+67:23:47.1	8	18.789	2.543	3.158
41	00:03:51.49	+67:31:22.3	9	19.545	1.926	2.573
42	00:04:09.21	+67:22:37.7	18	17.252	2.356	2.888
43	00:04:13.68	+67:24:45.7	55	18.563	2.876	3.292
44	00:04:18.14	+67:24:33.5	–	–	–	–
45	00:04:18.76	+67:26:27.1	–	–	–	–
46	00:04:20.31	+67:28:18.1	48	–	–	–
47	00:04:37.51	+67:28:55.5	41	–	–	–
48	00:04:09.21	+67:22:37.7	22	–	–	–

panel). Both NIR and optical data indicate an elongated morphology for the cluster.

#### 4.1.2 Radial stellar surface density profile

To find out the extent of the cluster, we used optical data of probable MS stars ( $V \leq 16$  and 18 mag) as well as 2MASS data ( $K \lesssim 14.3$ ). The centre of the cluster was determined using the stellar density distribution in a 100 pixel wide strip along both X and Y directions around an initially eye-estimated centre. The point of maximum density obtained by fitting Gaussian distribution is considered as

**Table 4.** List of IRAS point sources.

IRAS PSC	$\alpha_{2000}$ (h:m:s)	$\delta_{2000}$ (d:m:s)	$F_{12}$ (Jy)	$F_{25}$ (Jy)	$F_{60}$ (Jy)	$F_{100}$ (Jy)
23568+6706	23:59:25.81	67:23:39.1	5.80	9.75	184.0	841.0
00025+6708	00:05:07.39	67:24:45.0	0.79	1.38	16.6	73.9
00002+6647	00:02:47.50	67:03:47.2	0.77	1.31	13.0	59.5
00034+6658	00:06:06.31	67:15:27.0	0.90	1.72	18.4	68.5

the centre of cluster. The X, Y pixel coordinates of the cluster for optical data are found to be  $1128 \pm 7, 1024 \pm 13$ , respectively, which correspond to  $\text{RA}(2000) = 00^{\text{h}}02^{\text{m}}10^{\text{s}}.4 \pm 0^{\text{s}}.7$  and  $\text{Dec.}(2000) = 67^{\circ}25'10'' \pm 19''$ .

To determine the radial surface density, we divided the cluster into a number of concentric circles. Projected radial stellar density in each concentric annulus was obtained by dividing the number of stars by its area. Densities thus obtained are plotted in Fig. 3. The error bars are derived assuming that the number of stars in a concentric annulus follows the Poisson statistics. The horizontal dashed line in the plot indicates the density of contaminating field stars, which is obtained from the region (about 1.5 cluster radius) outside the cluster area. The extent of the cluster  $r_{\text{cl}}$  is defined as the point at which the radial density becomes constant and merges with the field star density. The radial extent of the cluster  $r_{\text{cl}}$  from optical data and NIR 2MASS data is estimated as  $\sim 10$  arcmin (2.9 pc) for a distance of 1.0 kpc.

The observed radial density profile (RDP) of the clusters was parametrized following the approach by Kaluzny & Udalski (1992) where the projected radial density  $\rho(r)$  is described as

$$\rho(r) = \frac{f_0}{1 + \left(\frac{r}{r_c}\right)^2},$$

where the core radius  $r_c$  is the radial distance at which the value of  $\rho(r)$  becomes half of the central density  $f_0$ . The best fit obtained by  $\chi^2$  minimization technique is shown in Fig. 3. Within the uncertainties, the model reproduces well the RDP of the cluster. The core radius  $r_c$  increases from  $1.0 \pm 0.1$  arcmin for  $V \leq 16$  mag to  $1.9 \pm 0.3$  arcmin for  $V \leq 18$  mag, whereas for the 2MASS data  $r_c$  comes out to be  $1.4 \pm 0.2$  arcmin. A closer look at the RDPs indicates a lack of stars in optical data in the  $5 < r < 8$  arcmin, whereas there seems an increase in the stellar density obtained from the 2MASS data in this radial distance range. This enhancement may be due to embedded population of low-mass stars.

#### 4.2 Interstellar extinction

The interstellar extinction in the cluster region is studied using the  $(U - B)/(B - V)$  two-colour diagram (TCD) shown in Fig. 4. In Fig. 4, the zero-age main sequence (ZAMS) from Schmidt-Kaler (1982) is shifted along a normal reddening vector having a slope of  $E(U - B)/E(B - V) = 0.72$ . A foreground population reddened by  $E(B - V) = 0.4$  mag can be noted easily. The TCD shows a variable reddening in the cluster region between  $E(B - V)_{\text{min}} \simeq 1.4$  and  $E(B - V)_{\text{max}} \simeq 1.8$  mag.

The reddening for the individual stars (those with photometric  $V_{\text{error}} \leq 0.1$  mag) with spectral type earlier than A0 has also been derived using the  $Q$  method (Johnson & Morgan 1953). The radial variation of reddening in the cluster region is shown in Fig. 5. The error bars represent standard errors. The reddening does not show any significant spatial variation in the cluster region barring a peak

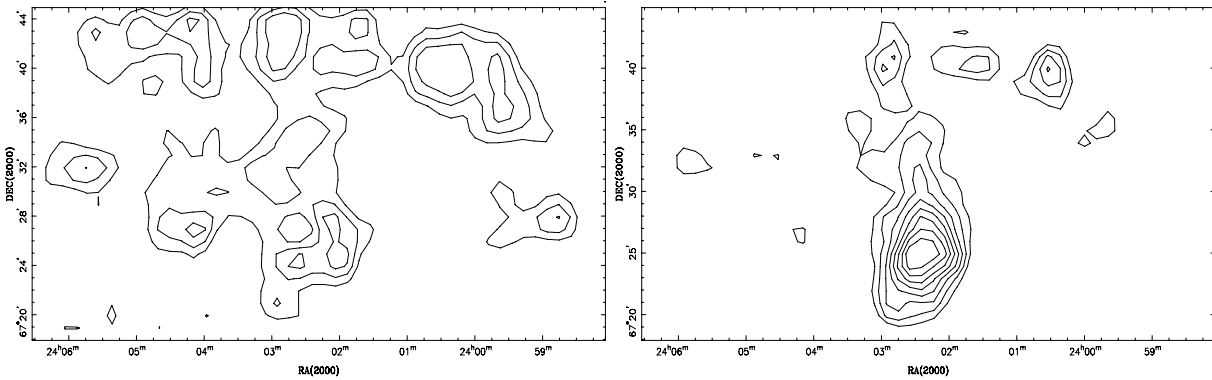


**Figure 2.** Left-hand panel: isodensity contours for stars having  $V \leq 18$  mag. Right-hand panel: isodensity contours for 2MASS stars in  $K_s$  band. The contours are plotted above  $3\sigma$  levels. For optical data, the contours have step size of  $5 \text{ stars pc}^{-2}$  with the lowest contour representing  $15 \text{ stars pc}^{-2}$ . The maximum stellar density is  $33 \text{ stars pc}^{-2}$ . For 2MASS data, the contours have step size of  $5 \text{ stars pc}^{-2}$  with lowest contour representing  $27 \text{ stars pc}^{-2}$ . The maximum stellar density is  $70 \text{ stars pc}^{-2}$ . The abscissa and the ordinate are for the J2000 epoch.

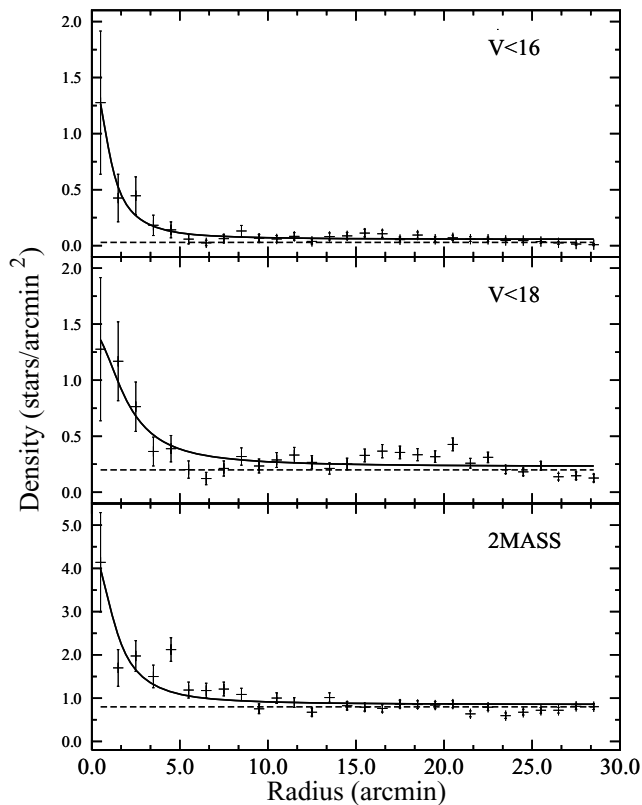


**Figure 3.** RDPs of probable MS stars of the cluster for different optical magnitude levels and 2MASS data. The continuous curve shows a least-square fit of the King (1962) profile to the observed data points. The error bars represent  $\pm\sqrt{N}$  errors. The dashed line indicates the density of field stars.

at  $r \sim 7.5$  arcmin. It may be interesting to point out that around the maxima of  $E(B - V)$  at  $r \sim 7.5$  arcmin, the optical RDP shows decrease in stellar density. The decrease in stellar density becomes more prominent if we include fainter stars in the sample. Whereas, at  $r \sim 7.5$  arcmin, the RDP from 2MASS data shows enhancement in the stellar density.

To study the nature of the extinction law in the cluster region, we used TCDs as described by Pandey et al. (2000, 2003). The TCDs of the form of  $(V - \lambda)$  versus  $(B - V)$ , where  $\lambda$  is one of the wavelengths

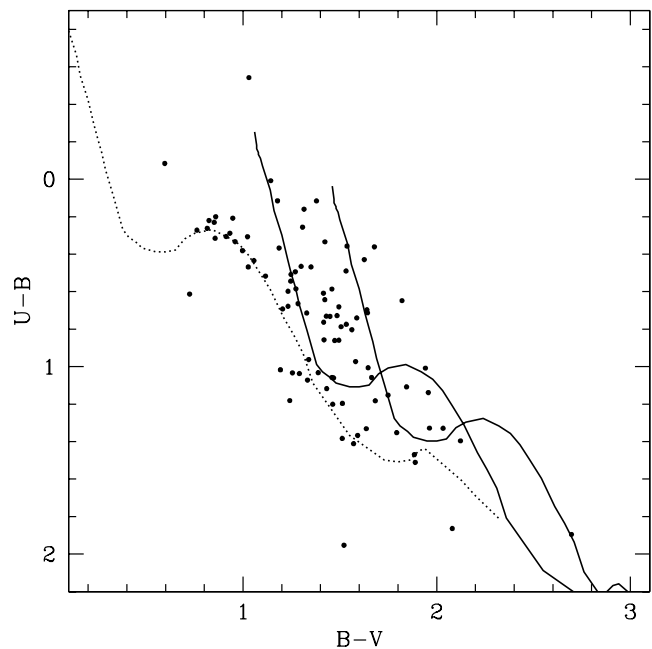


**Figure 4.** The  $(U - B)/(B - V)$  colour-colour diagram for the star within the region  $r < r_{cl}$ . The continuous curves represent ZAMS by Schmidt-Kaler (1982) shifted along the reddening slope of 0.72 for  $E(B - V) = 1.4$  and  $1.8$  mag, respectively. The dashed curve represents ZAMS shifted for the foreground reddening  $E(B - V) = 0.4$  mag.

of the broadband filters  $R$ ,  $I$ ,  $J$ ,  $H$ ,  $K$ , and  $L$  provides an effective method for separating the influence of the normal extinction produced by the diffuse interstellar medium from that of the abnormal extinction arising within regions having a peculiar distribution of dust sizes (cf. Chini & Wargau 1990; Pandey, Ogana & Sugitani 2000). The TCDs for the cluster region are shown in Fig. 6. The slopes of the distributions,  $m_{\text{cluster}}$  (cf. Pandey et al. 2003), are found to be  $1.34 \pm 0.08$ ,  $2.30 \pm 0.08$ ,  $2.90 \pm 0.11$ ,  $3.10 \pm 0.13$  for  $(V - I)$ ,  $(V - J)$ ,  $(V - H)$ ,  $(V - K)$  versus  $(B - V)$  diagrams, respectively. The ratios  $\frac{E(V - \lambda)}{E(B - V)}$  and the ratio of total-to-selective extinction in the cluster region,  $R_{\text{cluster}}$ , are derived using the procedure given by Pandey et al. (2003). The ratios  $\frac{E(V - \lambda)}{E(B - V)} (\lambda \geq \lambda_I)$  yield  $R_{\text{cluster}} = 3.7 \pm 0.3$  which indicates an anomalous reddening law. In the central region of Be 59, MacConnell (1968) has also found evidence

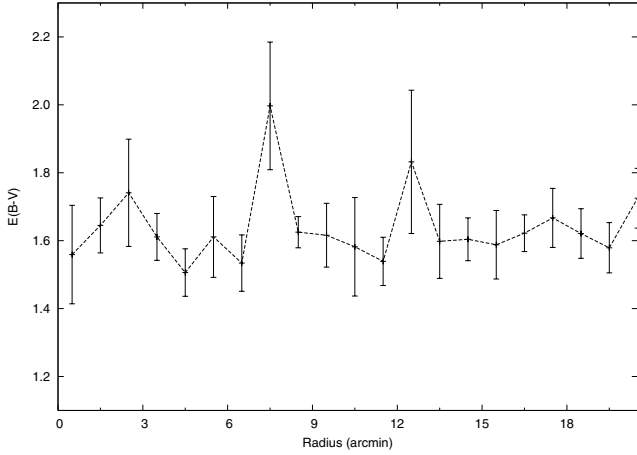


**Figure 5.** Radial distribution of the reddening from centre to outer region of the cluster. Error bars represent standard errors.

for large value (3.4–3.7) of  $R$ . Several studies have already pointed anomalous reddening law with high  $R$  value in the vicinity of star-forming regions (see e.g. Pandey et al. 2003, and references therein); however for the Galactic diffuse interstellar medium a normal value of  $R = 3.1$  is well accepted. The higher than the normal value of  $R$  has been attributed to the presence of larger dust grains. There is evidence that within dark clouds accretion of ice mantles on grains and coagulation due to colliding grains changes the size distribution towards larger particles. On the other hand, in star-forming regions, radiation from massive stars may evaporate ice mantles resulting in small particles. Here, it is interesting to mention that Okada et al. (2003), on the basis of the  $[\text{Si II}]$  35 to  $[\text{N II}]$  122  $\mu\text{m}$  ratio, suggested that efficient dust destruction is undergoing in the ionized region. Chini & Krügel (1983) and Chini & Wargau (1990) have shown that both – larger and smaller grains – may increase the ratio of total-to-selective extinction.

### 4.3 Optical colour–magnitude diagrams: distance, age and probable members of the cluster

Colour–magnitude diagram (CMD) for stars lying within the cluster region is shown in Fig. 7. The effect of field star contamination is

apparent in the CMDs of the outer/whole cluster region. The field population, which is reddened by  $E(B - V) = 0.4$  mag, is found to be located at  $\sim 470$  pc (see Fig. 7). Since foreground reddening [ $E(B - V)_{\text{min}} = 1.4$  mag] towards the cluster region is found to be normal, we used  $E(U - B)/E(B - V) = 0.72$ ,  $A_V = 3.1 \times E(B - V)$  and  $E(V - I) = 1.25 \times E(B - V)$  to visually fit the theoretical isochrone of 4 Myr ( $Z = 0.02$ ) by Bertelli et al. (1994) to the blue envelope of the observed MS of the cluster and found a distance modulus  $(m - M)_V = 14.35 \pm 0.10$  which corresponds to a distance of  $1.00 \pm 0.05$  kpc. The distance estimate is in agreement with that recently obtained by Sharma et al. (2007a).

To study the LF and MF, it is necessary to remove field star contamination from the sample of stars in the cluster region. Membership determination is also crucial for assessing the presence of pre-main-sequence (PMS) stars, because both PMS stars and dwarf foreground stars occupy similar positions above the ZAMS in the CMD. In the absence of proper motion study, we used statistical criterion to estimate the number of probable member stars in the cluster region.

Figs 8(a) and (b) show  $V$ ,  $(B - V)$  CMDs for the cluster and field regions, respectively. The contamination due to field population is clearly visible in the cluster region CMD. To remove contamination of field stars from the MS and PMS sample, we statistically subtracted the contribution of field stars from the CMD of the cluster region using following procedure. For any star in the  $V$ ,  $(B - V)$  CMD of the field region, the nearest star in the cluster’s  $V$ ,  $(B - V)$  CMD within  $V \pm 0.125$  and  $(B - V) \pm 0.065$  of the field star was removed. While removing stars from the cluster CMD, necessary corrections for incompleteness of the data samples were taken into account. The statistically cleaned  $V$ ,  $(B - V)$  CMD of the cluster region is shown in Fig. 8(c) which clearly shows the presence of PMS stars in the cluster. Fig. 9 shows statistically cleaned unreddened  $V_0$ ,  $(B - V)_0$  CMD where stars having spectral type earlier than A0 were individually dereddened (cf. Section 4.2), whereas the mean reddening, estimated from available individual reddening values in that region, was used for other stars. Since the cluster region shows anomalous reddening, the intrinsic magnitudes of stars having spectral type earlier than A0 were obtained as follows:

$$V_0 = V - [3.1 \times E(B - V)_{\text{min}} + R_{\text{cluster}} \times \Delta E(B - V)],$$

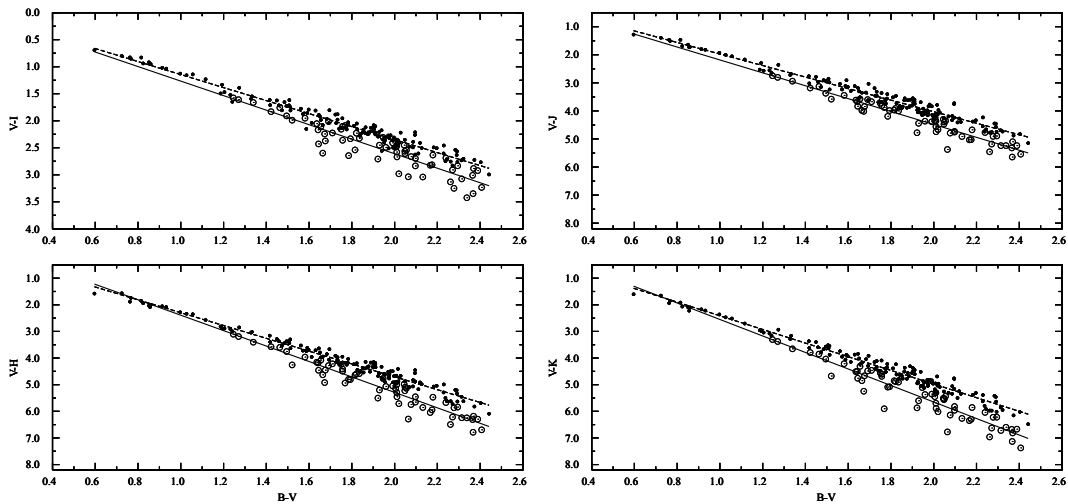


**Figure 6.**  $(V - I)$ ,  $(V - J)$ ,  $(V - H)$ ,  $(V - K)$  versus  $(B - V)$  TCDs within cluster region ( $r < r_{\text{cl}}$ ). Open and filled circles, respectively, represent probable cluster members with anomalous reddening and field stars with normal reddening. Straight lines show least-square fit to the data.

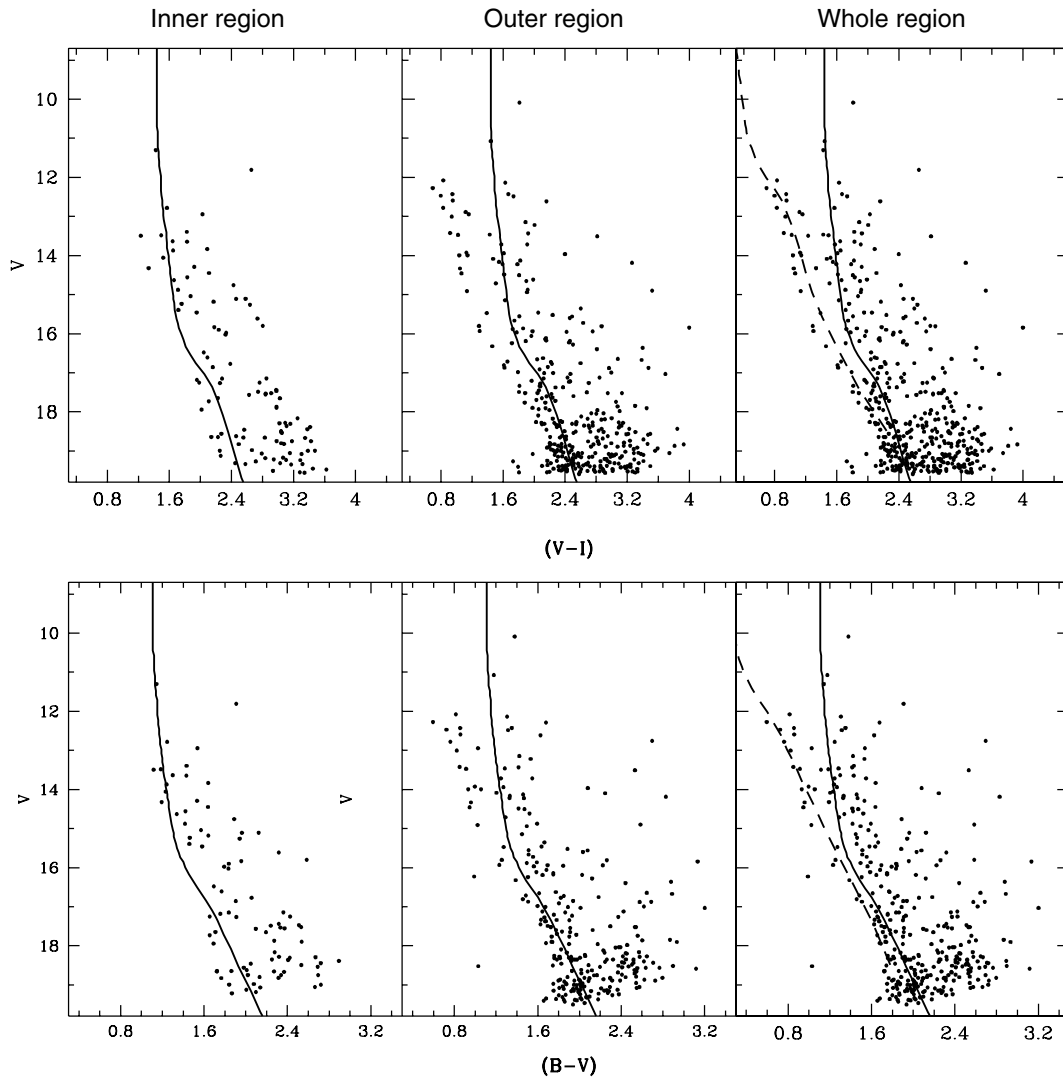


**Figure 7.** The CMDs for stars lying in the two subregions ( $r \leq 3$  arcmin and  $3 < r \leq 10$  arcmin) and whole cluster region. The isochrone by Bertelli et al. (1994) for solar metallicity and age of 4 Myr are also plotted for distance modulus of 14.35 mag and minimum reddening  $E(B - V) = 1.4$  mag. The dashed curve is ZAMS for  $E(B - V) = 0.4$  and distance modulus of 9.60 mag.

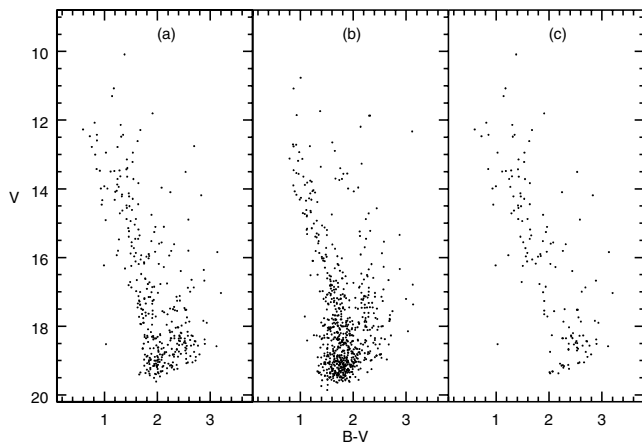


**Figure 8.**  $V$ ,  $(B - V)$  CMDs for (a) stars in the cluster region ( $r \leq 10$  arcmin), (b) stars in the field region and (c) statistically cleaned CMD of the cluster region.

where  $\Delta E(B - V) = E(B - V)_* - E(B - V)_{\min}$  and  $E(B - V)_*$  is  $E(B - V)$  value of individual stars estimated from the  $Q$  method.  $E(B - V)_{\min} = 1.4$  mag represents reddening due to diffuse normal interstellar matter. Proper motions of nine stars in the cluster region are available in the Webdata (WEBDA) (Mermilliod 1995). The membership probabilities along with star numbers from WEBDA are shown in Fig. 9. The photometric data for two stars (star number 3 and 4) are not available in the present sample, and so were taken from WEBDA. The O7 star (star number 4) in the region has a very low membership probability ( $p = 0.08$ ).

In Fig. 9, the ZAMS by Schmidt-Kaler (1982), isochrones for 4 Myr by Bertelli et al. (1994) and PMS isochrones by Siess, Dufour & Forestini (2000) have also been plotted. Fig. 9 yields an average post-main-sequence age of massive stars of the cluster as  $\sim 2$  Myr and also indicates a significant spread in the age of PMS stars. To check the reality of the age spread of PMS population, we plotted  $V$ ,  $(V - I)$  CMD for  $H\alpha$  emission stars and NIR excess stars (see Section 4.4) in Fig. 10, which also indicates an age spread of about  $\sim 1-5$  Myr for the PMS stars.

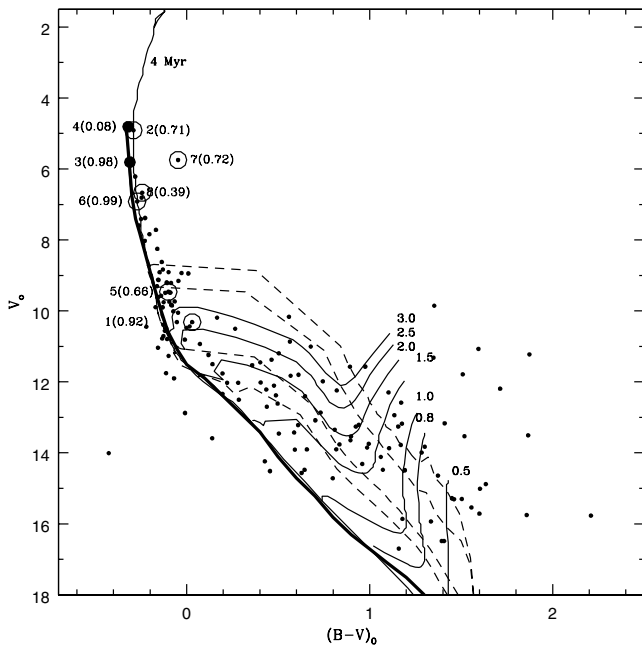


**Figure 9.** Statistically cleaned  $V_0$ ,  $(B - V)_0$  CMD for stars lying in the cluster region. The ZAMS (thick line) by Schmidt-Kaler (1982), isochrone (thin continuous line) for 4 Myr age by Bertelli et al. (1994) and PMS isochrones of 0.5, 1, 5, 10 Myr (dashed line) along with evolutionary tracks of different mass stars by Siess et al. (2000) are also shown. The MS and all the isochrones are corrected for a distance of 1 kpc. The stars shown by large open and filled circles have proper motion data. The star numbers are taken from WEBDA. The numbers in parentheses represent membership probability. The data for large filled circles are taken from WEBDA.

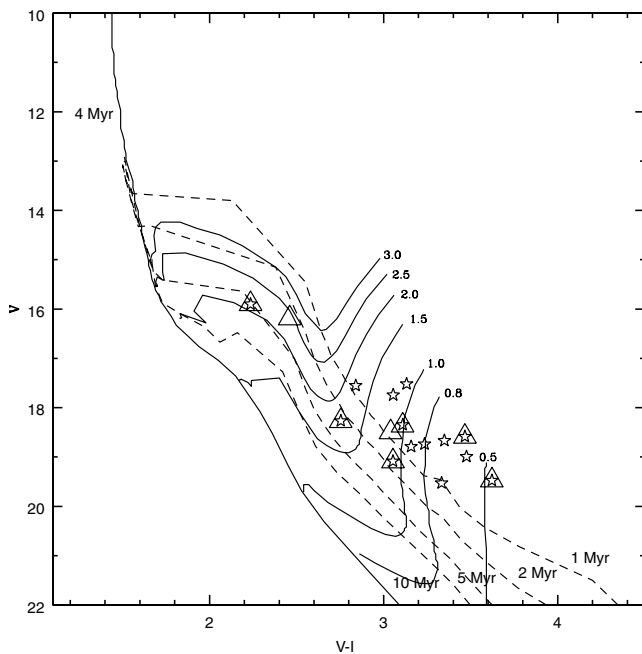


**Figure 10.**  $V$ ,  $(V - I)$  CMD for  $H\alpha$  emission stars (star symbols) and NIR excess stars (triangles). Isochrone for 4 Myr by Bertelli et al. (1994, continuous line) and PMS isochrones for 1, 2, 5, 10 Myr (dashed line) along with evolutionary tracks of different mass stars by Siess et al. (2000) are also shown. All the isochrones are corrected for distance of 1 kpc and reddening  $E(V - I) = 1.75$  mag which corresponds to  $E(B - V) = 1.4$  mag.

#### 4.4 NIR colour–colour and CMDs

NIR imaging surveys have emerged as a powerful tool to detect low-mass stars in star-forming regions. The  $(J - H)/(H - K)$  colour–colour diagrams for the cluster region ( $r < r_{cl}$ ) and for a nearby reference field are shown in Fig. 11. The solid and thick dashed curves represent the unreddened main-sequence and giant branch (Bessell & Brett 1988), respectively. The parallel dashed lines are the reddening vectors for early and giant stars (drawn from the base and tip of the two branches). The dotted line indicates the locus of T Tauri stars (TTs) (Meyer, Calvet & Hillenbrand 1997). The extinction ratios  $A_J/A_V = 0.265$ ,  $A_H/A_V = 0.155$  and  $A_K/A_V = 0.090$  have been taken from Cohen et al. (1981). All the 2MASS magnitudes and colours have been converted into the CIT system. The curves are also in the CIT system. We classified sources into three regions in the colour–colour diagram (cf. Ojha et al. 2004a). ‘F’ sources are located between the reddening vectors projected from the intrinsic colour of main-sequence stars and giants and are considered to be field stars (main-sequence stars, giants) or Class III/Class II sources with small NIR excesses. ‘T’ sources are located redward of region ‘F’ but blueward of the reddening line projected from the red end of the T Tauri locus of Meyer et al. (1997). These sources are considered to be mostly classical TTs (Class II objects) with large NIR excesses. There may be an overlap in NIR colours of Herbig Ae/Be stars and TTs in the ‘T’ region (Hillenbrand et al. 1992). ‘P’ sources are those located in the region redward of region ‘T’ and are most likely Class I objects (protostar-like objects; Ojha et al. 2004a). Here, it is worthwhile to mention that Robitaille et al. (2006) have recently shown that there is significant overlap between protostars and TTs in colour–colour space. Comparison of Figs 11(a) and (b) shows that the stars in the cluster region are distributed in a much wider range as compared to stars in the reference field. A significant number of the sources in the cluster region exhibit NIR excess emission, a characteristic of young stars with circumstellar material. Fig. 11(a) also shows a distribution of  $H\alpha$  emission stars.  $H\alpha$  emission stars are distributed in the ‘T’ and ‘F’ regions.

In Fig. 12(a)  $J$ ,  $(J - H)$  CMD is plotted for the stars within the cluster region. Fig. 12(b) shows statistically cleaned  $J$ ,  $(J - H)$  CMD obtained using the procedure described in Section 4.3. Using the relation  $\frac{A_J}{A_V} = 0.265$ ,  $\frac{A_{J-H}}{A_V} = 0.110$  (Cohen et al. 1981) and  $A_V = 3.1 \times E(B - V)$ , the isochrones for age 4 Myr by Bertelli et al. (1994) and PMS isochrones for ages 1, 10 Myr by Siess et al. (2000) have been plotted assuming a distance of 1.0 kpc and extinction  $E(B - V)_{min} = 1.4$  mag as obtained from the optical data. Probable TTs, obtained from the  $(J - H)/(H - K)$  colour–colour diagram and  $H\alpha$  emission stars, are shown by open triangles and star symbols, respectively, and indicate ages  $\leq 1$  Myr. The star numbers 3 (ID number is taken from WEBDA, Sp. type O9.5 V,  $p = 0.98$ ) and 6 (Sp. type B,  $p = 0.99$ ) lie leftward of the MS in the  $J$ ,  $(J - H)$  CMD, whereas on the  $V_0$ ,  $(B - V)_0$  CMD these stars lie on/near the MS. We presume that this scatter in  $J$ ,  $(J - H)$  CMD may be due to relatively large errors in NIR data. WEBDA star no. 7 ( $p = 0.72$ ) lies toward the right of 4 Myr isochrone in both the  $V_0$ ,  $(B - V)_0$  and  $J$ ,  $(J - H)$  CMDs. The  $(U - B)$  colour for this star is not available, therefore an average reddening of the region was applied. Recently, Sharma et al. (2007a) have carried out  $J$  and  $H$  photometry in the central region of Be 59. The WEBDA star no. 7 is located rightward of the 4 Myr isochrone in their  $J$ ,  $(J - H)$  CMD also. If this star is a cluster member, its evolutionary status does not match with the other massive stars in Be 59.

The mass of the probable YSO candidates can be estimated by comparing their locations on the NIR CMD with the evolutionary

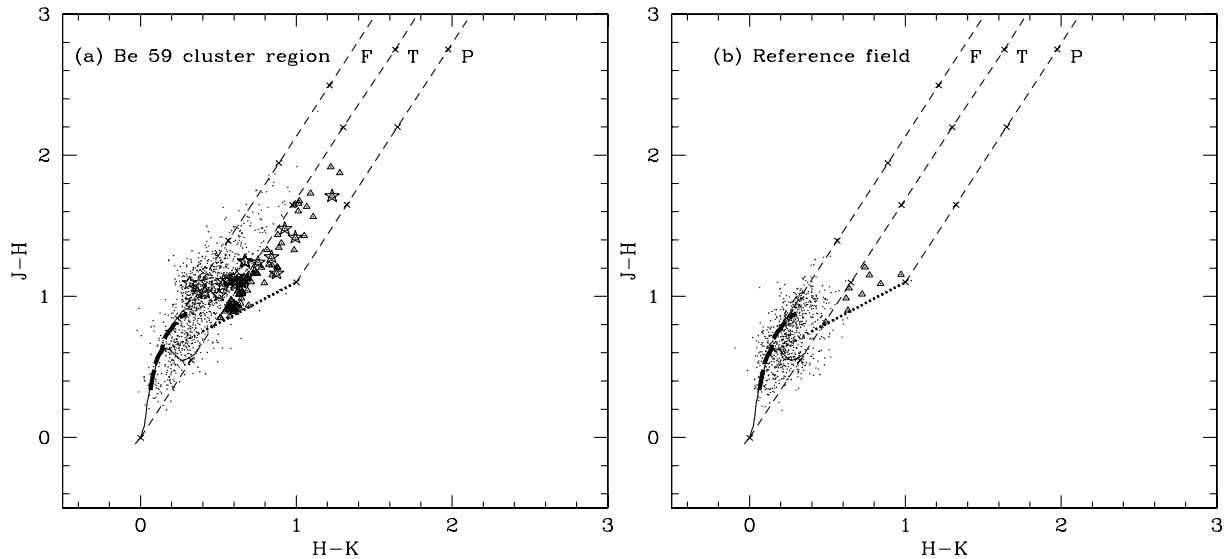


**Figure 11.**  $(J - H)/(H - K)$  colour–colour diagrams of sources detected in the  $JHK_s$  bands with photometric errors less than 0.1 mag in (a) the cluster region ( $r \leq r_{cl}$ ) and (b) the reference field. The sequences for dwarfs (solid curve) and giants (thick dashed curve) are from Bessell & Brett (1988). The dotted line represents the locus of TTS (Meyer et al. 1997). Dashed straight lines represent the reddening vectors (Cohen et al. 1981). The crosses on the dashed lines are separated by  $A_V = 5$  mag. The star symbols are the  $H\alpha$  emission stars detected from slitless spectroscopy. Open triangles are probable TTSs.

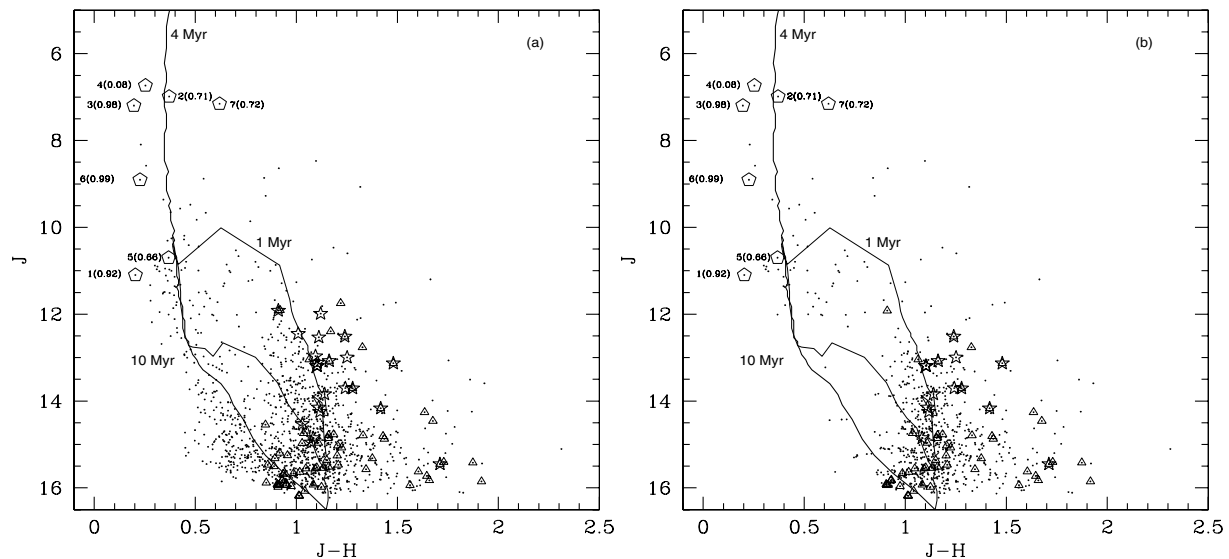


**Figure 12.** (a)  $J, (J - H)$  CMD of the stars within cluster region ( $r \leq r_{cl}$ ). The symbols are the same as in Fig. 11. The isochrone of 4 Myr ( $Z = 0.02$ ) by Bertelli et al. (1994) and PMS isochrones of age 1 and 10 Myr by Siess et al. (2000) corrected for a distance of 1 kpc and the minimum reddening  $E(B - V)_{\min} = 1.4$  mag are also shown. The star numbers are taken from WEBDA. The numbers in parentheses represent membership probability. (b) Same as (a) but statistically cleaned  $J, (J - H)$  CMD.

models of PMS stars. To estimate the stellar masses, the  $J$  luminosity is recommended rather than that of  $H$  or  $K$ , as the  $J$  band is less affected by the emission from circumstellar material (Bertout, Basri & Bouvier 1988). Fig. 13 shows  $J, (J - H)$  CMD for probable YSO candidates identified in Fig. 11. The solid curve, taken from Siess et al. (2000), denotes the loci of 1 Myr old PMS stars having masses in the range of 0.1 to  $3.5 M_{\odot}$ . The majority of YSOs have masses in the range 3.0 to  $0.1 M_{\odot}$ .

#### 4.5 Initial MF and K-band LF

The distribution of stellar masses that form in a star formation event in a given volume of space is called IMF. Young embedded clusters

are important tools to study the IMF as their MF can be considered as the IMF since they are too young to lose a significant number of members either by dynamical or by stellar evolution. The MF is often expressed by a power law,  $N(\log m) \propto m^{\Gamma}$ , and the slope of the MF is given as

$$\Gamma = d \log N(\log m) / d \log m,$$

where  $N(\log m)$  is the number of stars per unit logarithmic mass interval. The classical value derived by Salpeter (1955) is  $\Gamma = -1.35$ .

With the help of statistically cleaned CMD, shown in Fig. 9, we can derive the MF using the theoretical evolutionary model of Bertelli et al. (1994). Here, we would like to remind that necessary

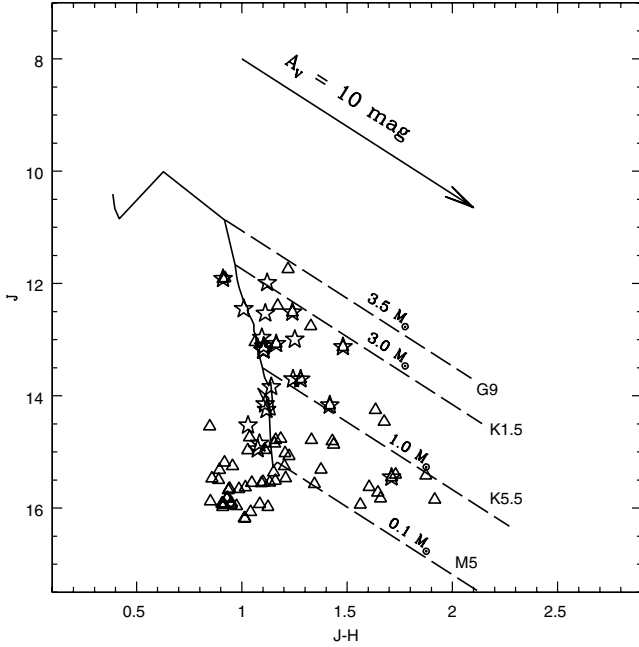


**Figure 13.**  $J$ ,  $(J - H)$  CMD for the YSO candidates in cluster region ( $r \leq r_{cl}$ ). The symbols are the same as in Fig. 11. The solid curve denotes PMS isochrone of 1 Myr, derived from Siess et al. (2000) and corrected for a distance of 1 kpc. Masses range from 3.5 to  $0.1 M_{\odot}$  from top to bottom. The dashed oblique reddening lines are for PMS stars of 0.1, 1, 3.0 and  $3.5 M_{\odot}$  from bottom to top.

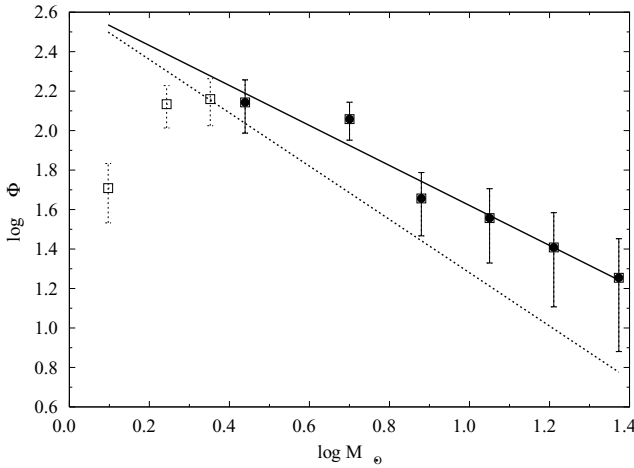


**Figure 14.** A plot of the MF in the cluster.  $\log \phi$  represents  $\log(N/d \log m)$ . The error bars represent  $\pm\sqrt{N}$  errors. The continuous line shows a least-square fit to the mass range  $2.5 < M/M_{\odot} < 28$ . The dashed line represents MF having Salpeter value  $\Gamma = -1.35$ .

corrections for the incompleteness of the data sample have been taken into account to get the statistically cleaned CMD. Since post-main-sequence age of the cluster is  $\sim 2$  Myr, the stars having  $V < 15$  mag ( $V_0 < 10$ ;  $M > 4 M_{\odot}$ ) have been considered on the MS. For the MS stars, the LF was converted to MF using the theoretical model by Bertelli et al. (1994) (cf. Pandey et al. 2000, 2005). The MF for PMS stars was obtained by counting the number of stars in various mass bins (shown as evolutionary tracks) in Fig. 9. The MF of the cluster is plotted in Fig. 14. The slope of the MF  $\Gamma$  in the mass range  $2.5 < M/M_{\odot} < 28$  comes out to be  $-1.01 \pm 0.11$ , which is shallower than the Salpeter value ( $-1.35$ ). A turn-off in the MF can

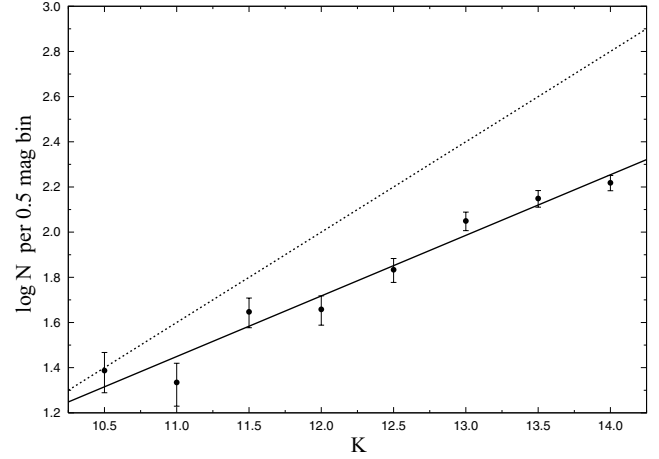


**Figure 15.** The corrected KLF for the probable members in the cluster. The star counts are number of stars per 0.5 mag bin and the error bars represent  $\pm\sqrt{N}$  errors. The continuous line is the least-square fit to the data points in the mag range 10.5–14.0. The value of the power-law slope  $\alpha$  is  $0.27 \pm 0.02$ . Dashed line having slope  $\alpha = 0.4$  represents the average KLF for young clusters (see text).

be seen at  $\sim 2.5 M_{\odot}$ . In the mass range  $1.5 < M/M_{\odot} < 2.5$ , the MF is almost flat ( $\Gamma \sim 0$ ). The shallower MF for Be 59 obtained in the present study does not support a universal IMF.

The  $K$ -band luminosity function (KLF) is a powerful tool to investigate the IMF of young embedded star clusters; therefore during the last decade several studies have focused on the determination of the KLF of young open clusters (e.g. Lada & Lada 2003; Ojha et al. 2004b; Sanchawala et al. 2007). In order to obtain the KLF, we have to examine the effects of incompleteness and field star contamination in our data. The completeness of the data is estimated using the ADDSTAR routine of DAOPHOT as described in Section 2.1. To take into account foreground/background field star contamination, we used both the Besançon Galactic model of stellar population synthesis (Robin et al. 2003) and nearby reference star field. Star counts are predicted using the Besançon model in the direction of the control field. We checked the validity of the simulated model by comparing the model KLF with that of the control field and found that both the KLFs match rather well. An advantage of using the model is that we can separate the foreground ( $d < 1.0$  kpc) and the background ( $d > 1.0$  kpc) field stars. The foreground extinction is found to be  $A_V \sim 4.3$  mag (cf. Section 4.2). Model simulations with  $A_V = 4.3$  mag and  $d < 1.0$  kpc give the foreground contamination. The background population ( $d > 1.0$  kpc) was simulated with  $A_V = 6.7$  mag. We thus determined the fraction of the contaminating stars (foreground+background) over the total model counts. This fraction was used to scale the nearby reference field, and subsequently the star counts of the modified control field were subtracted from the KLF of the cluster to obtain the final corrected KLF. The KLF is expressed by the following power law:

$$\frac{dN(K)}{dK} \propto 10^{\alpha K}$$

where  $\frac{dN(K)}{dK}$  is the number of stars per 0.5 mag bin and  $\alpha$  is the slope of the power law. Fig. 15 shows the KLF for the cluster region which indicates a slope of  $\alpha = 0.27 \pm 0.02$  which is smaller than the average value of slopes ( $\alpha \sim 0.4$ ) for young clusters (Lada et al. 1991; Lada & Lada 1995, 2003). Smaller values ( $\sim 0.3$ – $0.2$ ) have been reported for various young embedded clusters (e.g. Megeath et al. 1996; Chen, Tafalla & Greene 1997; Brandl, Brandner & Eisenhauer 1999; Ojha

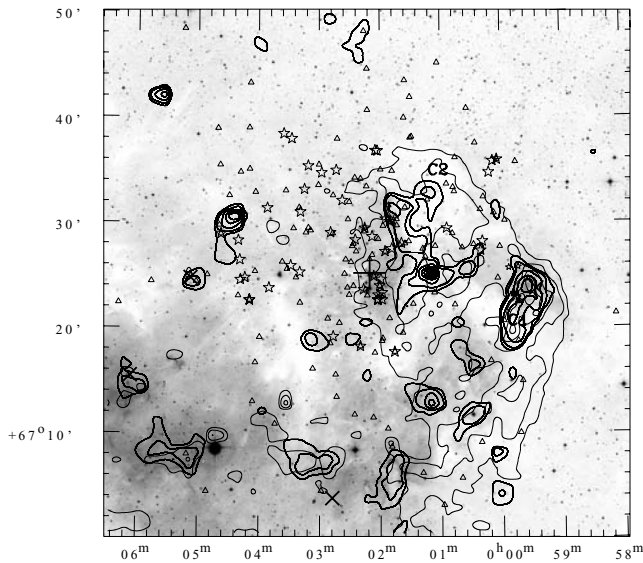


**Figure 16.** Spatial distribution of IR-excess sources (open triangles),  $H\alpha$  (star symbols) and *IRAS* point sources (crosses) is overlaid on DSS-II *R*-band image. NVSS (1.4 GHz) radio contours (thick contours) and MSX A-band intensity contours (thin contours) have also been shown. The contours are 2, 4, 10, 20, 30, 40, 50, 60, 70, 80 and 90 per cent of the peak value  $134.6 \text{ mJy beam}^{-1}$  for NVSS and 5, 10, 20, 30, 40, 50, 60, 70, 80 and 90 per cent of the peak value  $2.9 \times 10^{-5} \text{ W m}^{-2} \text{ Sr}^{-1}$  for MSX A-band contours, respectively. The abscissa and the ordinates are for the J2000 epoch. C1 and C2 represent the locations of the peaks of molecular clumps (see Yang & Fukui 1992 for details). The plus mark represents the optical centre of the cluster.

et al. 2004b; Leistra et al. 2005; Sanchawala et al. 2007). Since the IMF for Be 59 is found to be shallower ( $\Gamma = -1.01 \pm 0.11$ ) than the Salpeter value, the low value of the slope of the KLF of Be 59 may be an intrinsic property of the Be 59 region.

Recently, we have studied the IMF and KLF for another young cluster (age  $\sim 4$  Myr) NGC 1893 (Sharma et al. 2007b) and it is worthwhile to compare the IMF/KLF estimates of NGC 1893 with those obtained for Be 59. The mass–luminosity relation  $L_K \propto m^\beta$ , KLF and MF i.e.  $N(\log m) \propto m^\Gamma$  yield relation  $\alpha = \frac{-\Gamma}{2.5\beta}$ , where  $\alpha$ ,  $\Gamma$  and  $\beta$  are the slopes of the KLF, IMF and mass–luminosity relation, respectively (Lada et al. 1993). The values of  $\Gamma$  ( $-1.01 \pm 0.11$  in the mass range  $2.5 \leq M/M_\odot \leq 28$  for Be 59;  $-1.27 \pm 0.08$  in the mass range  $0.6 \leq M/M_\odot \leq 18$  for NGC 1893) and  $\alpha$  ( $0.27 \pm 0.02$  for Be 59;  $0.34 \pm 0.07$  for NGC 1893) yield  $\beta \sim 1.5$  for both the clusters which are in between the values reported for massive OB-type stars ( $\beta = 2$ ) and PMS stars ( $\beta = 1$ ).

## 5 STAR FORMATION SCENARIO AROUND THE STAR CLUSTER

The distribution of YSOs and morphological details of the environment around the cluster containing OB stars can be used to probe the star formation history of the region. The OB-type stars in the cluster region produce UV radiation that ionizes its surroundings, consequently IF is generated. The IF drives a shock into the pre-existing molecular clumps and compresses it, consequently the clumps become gravitationally unstable and collapse to form next-generation stars (Elmegreen 1989, 1998). Fig. 16 shows the spatial distribution of NIR-excess sources and  $H\alpha$  emission stars, both being probable TTSs, on a  $50 \times 50$  arcmin<sup>2</sup> DSS-II *R*-band image. The major-

ity of NIR-excess and  $H\alpha$  emission stars are distributed along the elongated morphology of the cluster as well as towards east of the cluster. Yang & Fukui (1992) studied the S171 region and identified two dense molecular clumps (C1 and C2) near the cluster Be 59. The radial velocities of the clumps  $V_{\text{LSR}} = -14.4 \text{ km s}^{-1}$  (C1) and  $-16.0 \text{ km s}^{-1}$  (C2) are comparable with the radial velocity of member stars of Be 59 ( $V_{\text{LSR}} = -15.7 \text{ km s}^{-1}$ ), which indicate that the clumps are associated with the cluster. They further found high degree of spatial correlation between the ionized and molecular gas suggesting that these are physically associated. On the basis of the physical association of the molecular clumps, the cluster and the ionized gas, Yang & Fukui (1992) concluded that a new generation of stars could be expected in the compressed gas layer.

The clump C1 harbours the bright-rimmed cloud BRC1 (cf. Sugitani, Fukui & Ogura 1991). BRCs in  $H\text{II}$  regions are potential sites of ongoing star formation due to the radiation driven implosion (RDI), where shock front associated with the IF compresses the cloud and causes the BRC to collapse. Morgan et al. (2004, 2006) studied the internal molecular pressure and external ionized boundary layer pressure for nine BRCs, and in the case of BRC1 found that the external pressure is greater than the internal pressure of the molecular cloud which indicates that the IF is compressing the molecular gas. In fact, Ogura et al. (2002) have detected six  $H\alpha$  stars in the vicinity of BRC1 which can be interpreted as second generation of formation of low-mass stars due to RDI.

In Fig. 16, the NRAO VLA Sky Survey (NVSS) (1.4 GHz) radio continuum emission contours (thick line) and MSX A-band (8  $\mu\text{m}$ ) mid-infrared (MIR) contours (thin line) are overlaid on a DSS-II *R*-band image. The locations of the *IRAS* point sources are shown by crosses, and the C1 and C2 clumps of Yang & Fukui (1992) are also marked. The peaks of the radio continuum and that of the MSX A-band emission around clump C1 coincide very well. The clump C1 also harbours an *IRAS* source which is located in BRC1. Another peak of radio continuum at RA (2000) =  $00^{\text{h}}01^{\text{m}}12^{\text{s}}$ , Dec. (2000) =  $67^{\circ}25'00''$  lies near the clump C2. The emission from MSX A band is more extended towards the west side of the cluster, whereas it is completely absent towards east of the cluster.

The contribution of UIBs due to polycyclic aromatic hydrocarbons (PAHs) to the mid-infrared emissions in the MSX bands has been studied using the scheme developed by Ghosh & Ojha (2002). The emission from each pixel is assumed to be a combination of two components, namely the thermal continuum from dust grains (grey body) and the emission from the UIB features in the MSX bands. The scheme assumes a dust emissivity of the power law form  $\epsilon_\lambda \propto \lambda^{-1}$  and the total radiance due to the UIBs in band *C* is proportional to that in band *A*. A self-consistent non-linear chi-square minimization technique is used to estimate the total emission from the UIBs and the warm dust optical depth. The spatial distribution of the UIB emission and optical depth ( $\tau_{10}$  at 10  $\mu\text{m}$ ) contour maps with an angular resolution of  $\sim 18$  arcsec (for the MSX survey) extracted for the cluster region are shown in Fig. 17. The peaks of the UIB emissions are located at the western border of the radio continuum emission around the clump C1 (see Fig. 17) which indicates an interface between the ionized and molecular gas. The peak of the  $\tau_{10}$  optical depth lies at  $\sim 4$  arcmin away towards SW of the cluster centre.

Fig. 18 shows the *IRAS-HIRES* intensity maps for the cluster region where emission shows a strong peak at the clump C1. Another peak towards south-west of the cluster Be 59 can also be noted. *IRAS-HIRES* maps were also used to generate the spatial distribution of dust optical depth at 25  $\mu\text{m}$  ( $\tau_{25}$ ) and 100  $\mu\text{m}$  ( $\tau_{100}$ ), using the procedure given by Ghosh et al. (1993). An emissivity law of

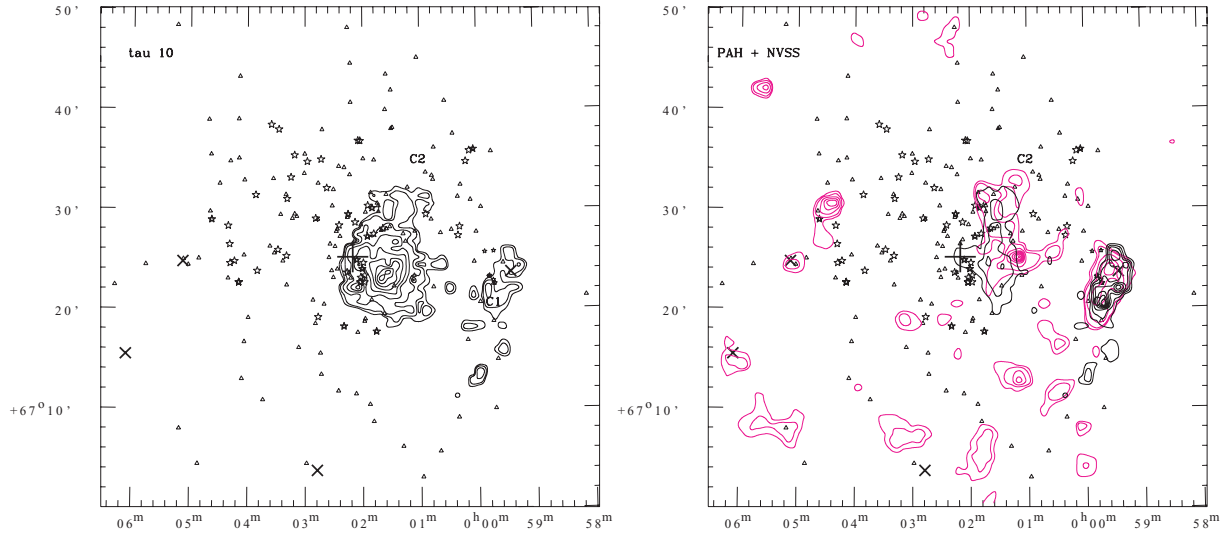


**Figure 17.** Left-hand panel: distribution of optical depth ( $\tau_{10}$  at  $10\ \mu\text{m}$ ) around the cluster region. The contours are at 3, 5, 10, 20, 30, 40, 50, 60, 70, 80 and 90 per cent of the peak value of  $5.5 \times 10^{-5}$ . Right-hand panel: emission in UIBs (thick contours) and radio continuum (1.4 GHz, thin contours). For UIBs, the contours are at 10, 20, 30, 40, 50, 60, 70, 80 and 90 per cent of the peak value of  $1.2 \times 10^{-5}\ \text{W m}^{-2}\ \text{Sr}^{-1}$ . The contour levels for radio continuum and the symbols are the same as in Fig. 16. The abscissa and the ordinates are in the J2000 epoch.

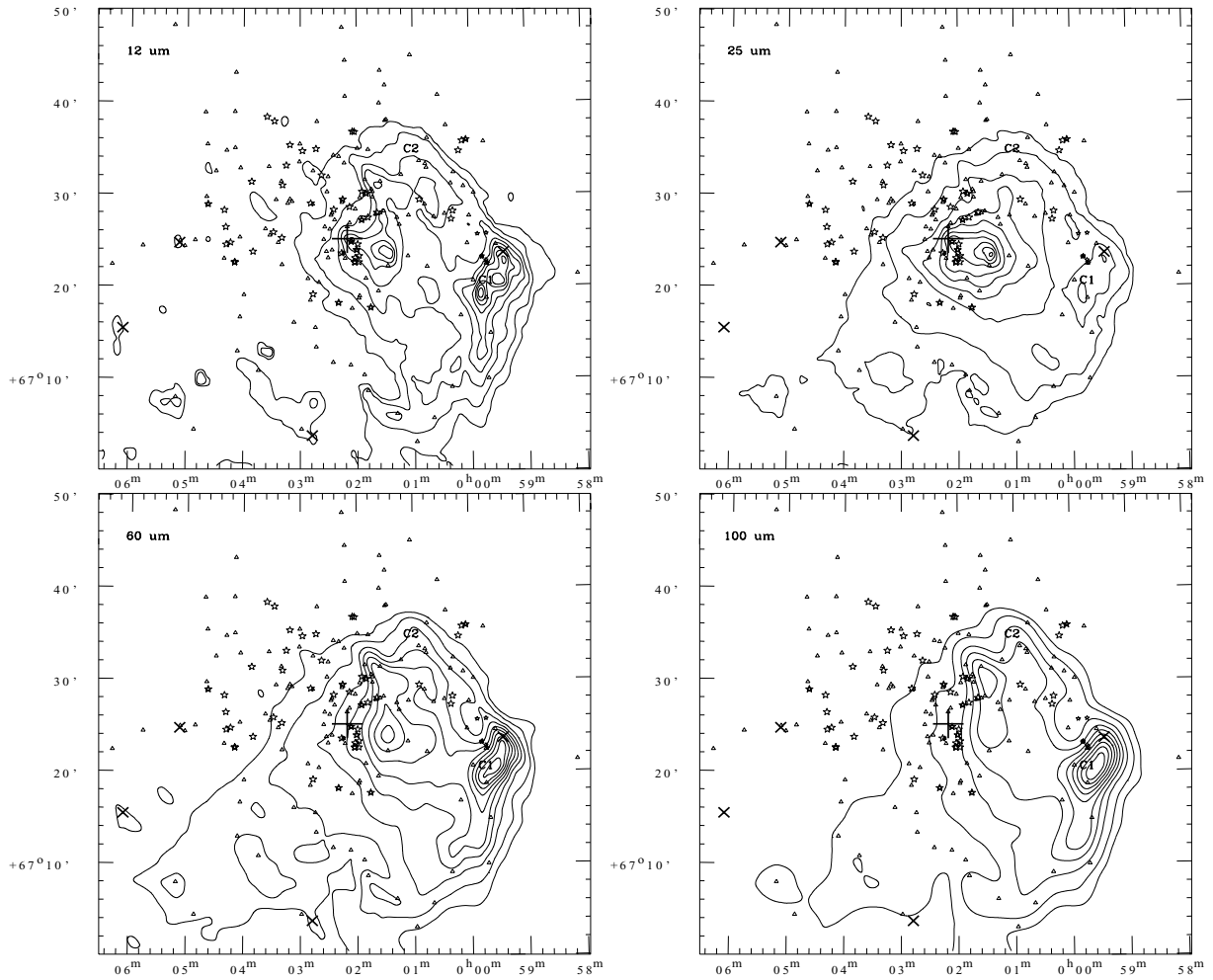


**Figure 18.** The *IRAS-HIRES* intensity maps for the cluster region at  $12\ \mu\text{m}$  (top left),  $25\ \mu\text{m}$  (top right),  $60\ \mu\text{m}$  (bottom left) and  $100\ \mu\text{m}$  (bottom right). The contours are at 5, 10, 20, 30, 40, 50, 60, 70, 80 and 90 per cent of the peak value of 116, 445, 1560 and 2715 MJy/ster at 12, 25, 60 and 100  $\mu\text{m}$ , respectively. The symbols are the same as in Fig. 16.

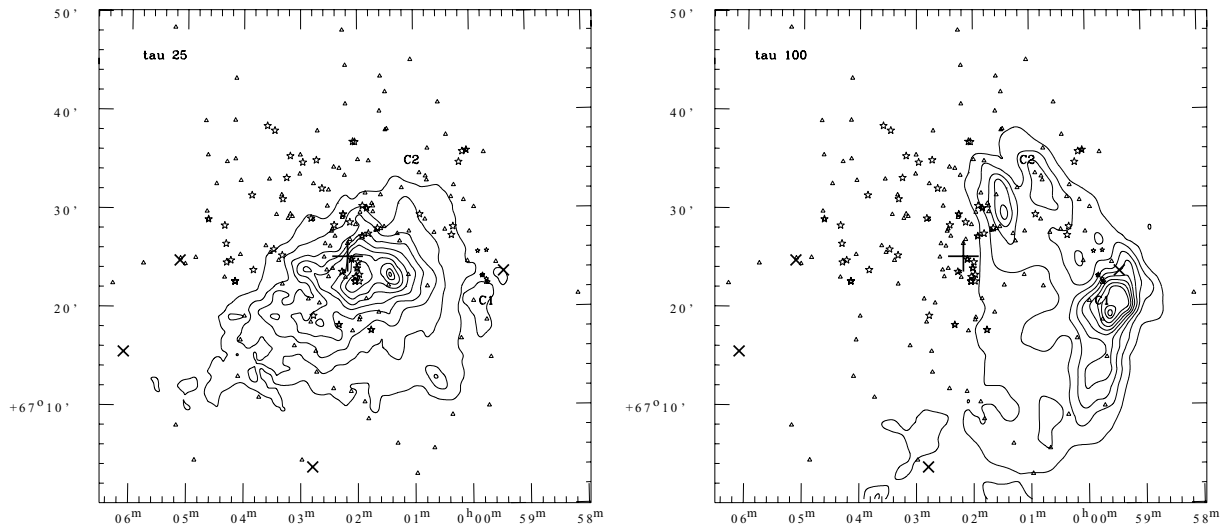


**Figure 19.** Left-hand panel: the dust optical depth ( $\tau_{25}$ ) distribution from the *HIRES* 12 and 25  $\mu\text{m}$  maps assuming a dust emissivity law of  $\epsilon_\lambda \propto \lambda^{-1}$ . The contours represent 10, 20, 30, 40, 50, 60, 70, 80, 90 and 95 per cent of the peak value of  $1.09 \times 10^{-5}$ . Right-hand panel: the dust optical depth ( $\tau_{100}$ ) distribution from the *HIRES* 60 and 100  $\mu\text{m}$  maps. The contours represent 10, 20, 30, 40, 50, 60, 70, 80, 90 and 95 per cent of the peak value of  $3.83 \times 10^{-3}$ . The abscissa and the ordinates are in J2000 epoch.

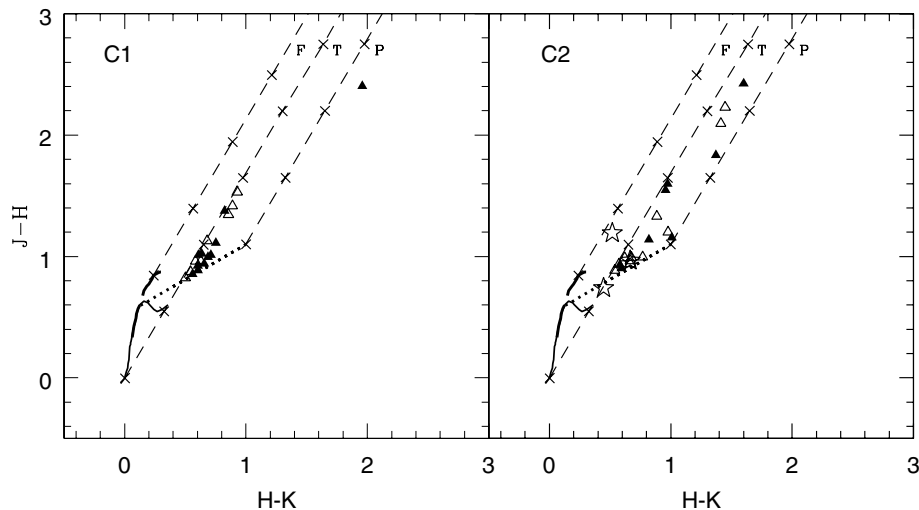


**Figure 20.**  $(J - H)/(H - K)$  CMD for the YSO candidates around the clumps C1 and C2. The star symbols and triangles are  $H\alpha$  emission and NIR excess stars, respectively. Filled triangles are stars having photometric errors between 0.1 and 0.2 mag.

$\epsilon_\lambda \propto \lambda^{-1}$  was assumed to generate these maps. The optical depth maps representing warmer (25  $\mu\text{m}$ ) and cooler dust (100  $\mu\text{m}$ ) components are presented in Fig. 19. The warm dust ( $\tau_{25}$ ) is mainly distributed towards east of the clump C1 around the Be 59 cluster position as well as SE and SW of Be 59, whereas the cold dust ( $\tau_{100}$ ) emission is seen west of Be 59 cluster and shows peaks around the clumps C1 and C2. The spatial correlation between the ionized gas, molecular gas and dust around the clumps C1 and C2 suggests that these clumps may be the locations of second-generation star formation as suggested by Yang & Fukui (1992). The morphology of the MSX A band as well as *IRAS* intensity maps implies that the H II region is ionization bounded towards the western side of the cluster.

A comparison is also made between the  $\tau_{10}$  maps generated from the higher angular resolution MSX maps (Fig. 17) and that based on the *IRAS-HIRES* maps at 12 and 25  $\mu\text{m}$ . The latter ( $\tau_{25}$ ) is shown in Fig. 19 which was scaled to 10  $\mu\text{m}$  assuming a  $\lambda^{-1}$  emissivity law to compare with the MSX  $\tau_{10}$  map. The peak optical depth is

$5.49 \times 10^{-5}$  for the map based on MSX. The corresponding value from the *IRAS-HIRES* maps is  $2.73 \times 10^{-5}$ . These derived values are in reasonable agreement considering that they are based on instruments with very different angular resolutions. The difference in the peak values of  $\tau_{10}$  may be a result of the following effects: beam dilution, clumpy interstellar medium and the contribution of UIB emission. In particular, the contribution of the UIBs emission has been removed in generating the optical depth in the modelling of the MIR emission from the MSX bands; however the *IRAS-HIRES* maps represent the emission from dust and UIB carriers [e.g. the emission from the UIB features falls within the *IRAS* 12  $\mu\text{m}$  band ( $\sim 8\text{--}15 \mu\text{m}$ )]. The overestimate of thermal emission from the grains at 12  $\mu\text{m}$  band due to UIB features would imply a higher effective colour temperature  $T(12/25)$  for the grains. This would then affect the inferred optical depth (by reduction in its value).

The  $(J - H)/(H - K)$  colour-colour diagrams for the probable YSOs lying around the clumps C1 and C2 are shown in Fig. 20.

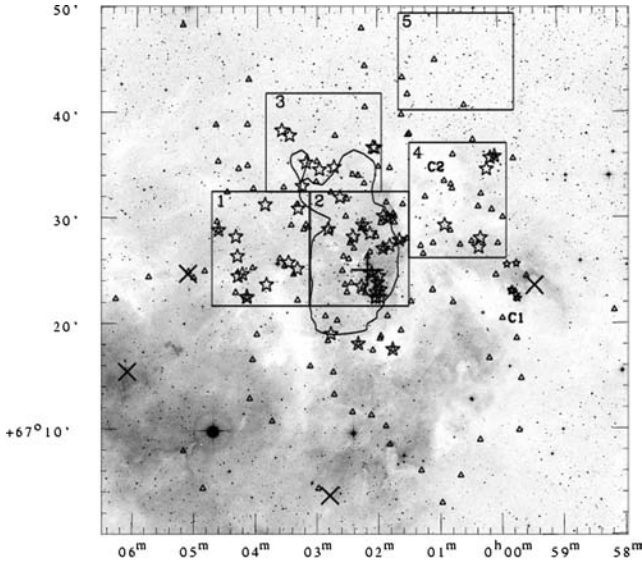


**Figure 21.** Five selected sub-regions overlaid on DSS-II *R*-band image. The symbols are the same as in Fig. 16. The abscissa and the ordinates are for the J2000 epoch. The continuous curve represents the outer most 2MASS  $K_s$ -band isodensity contour (see Fig. 2, right-hand panel).

Since the clump regions are associated with higher extinction, we also used data of those stars having photometric errors in the range 0.1–0.2 mag to improve the statistics. The stars having error larger than 0.1 mag are shown by filled triangles in Fig. 20. A comparison of Fig. 20 with the cluster region colour–colour diagram (Fig. 11) indicates that stars lying in the clump C2 have higher extinction and relatively larger NIR excess suggesting that these stars may be younger than the stars in the clump C1 and cluster region. If this is true, then star formation in the clump regions might have taken place as a result of triggering as suggested by Yang & Fukui (1992).

To study the age sequence, if any, we selected four sub-regions (regions 1–4) in/around the cluster region and a field region (Region 5) outside the cluster as shown in Fig. 21. Fig. 22 shows  $(J - H)/(H - K)$  colour–colour diagrams of YSOs in the four sub-regions and the field region. The NIR excess stars and  $H\alpha$  stars are shown by open triangles and star symbols, respectively. The statistics are given in Table 5, which manifest that regions 1 and 4 have higher percentage of YSOs as compared to the regions 2 and 3 which lie in the cluster. This indicates that the regions 1 and 4 should be younger than the cluster. Fig. 23 shows dereddened  $V_0$ ,  $(V - I)_0$  CMDs for the probable YSOs (NIR excess and  $H\alpha$  emission stars) along with stars on/near the MS (filled circles) in regions 1, 2 and 3. The  $(J - H)/(H - K)$  TCD was used to estimate  $A_V$  for each YSO by tracing back to the intrinsic line by Meyer et al. (1997) along the

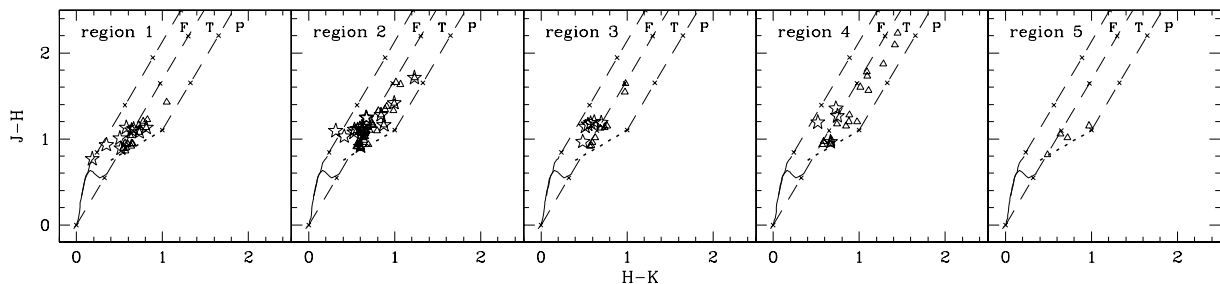


**Figure 22.**  $(J - H)/(H - K)$  CMD for the YSO candidates in five selected regions. The symbols are the same as in Fig. 11.

**Table 5.** Statistics of YSOs in four sub-regions. Numbers given in parentheses are in percentage of probable cluster members.

Region	Total stars	NIR excess stars	$H\alpha$ stars	All YSOs
1	288	15 (50)	9 (41)	18 (82) <sup>b</sup>
2	686	33 (7)	16 (4)	40 (10) <sup>c</sup>
3	358	9 (5)	6 (7)	11 (12)
4	229	17 (100) <sup>a</sup>	4 (100) <sup>a</sup>	16 (100) <sup>d</sup>
Field	266	4		

<sup>a</sup>Total stars in Region 4 are less than the field region, therefore all the stars in Region 4 are considered as NIR excess/ $H\alpha$  stars.

<sup>b</sup>Two  $H\alpha$  stars have NIR excess.

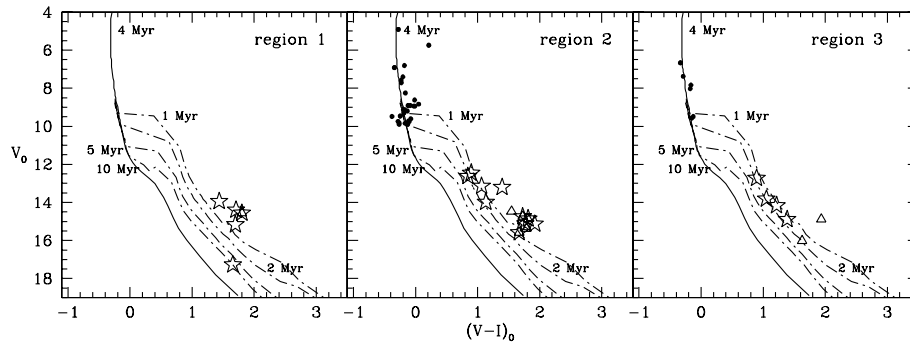
<sup>c</sup>Five  $H\alpha$  stars have NIR excess.

<sup>d</sup>One  $H\alpha$  star has NIR excess.

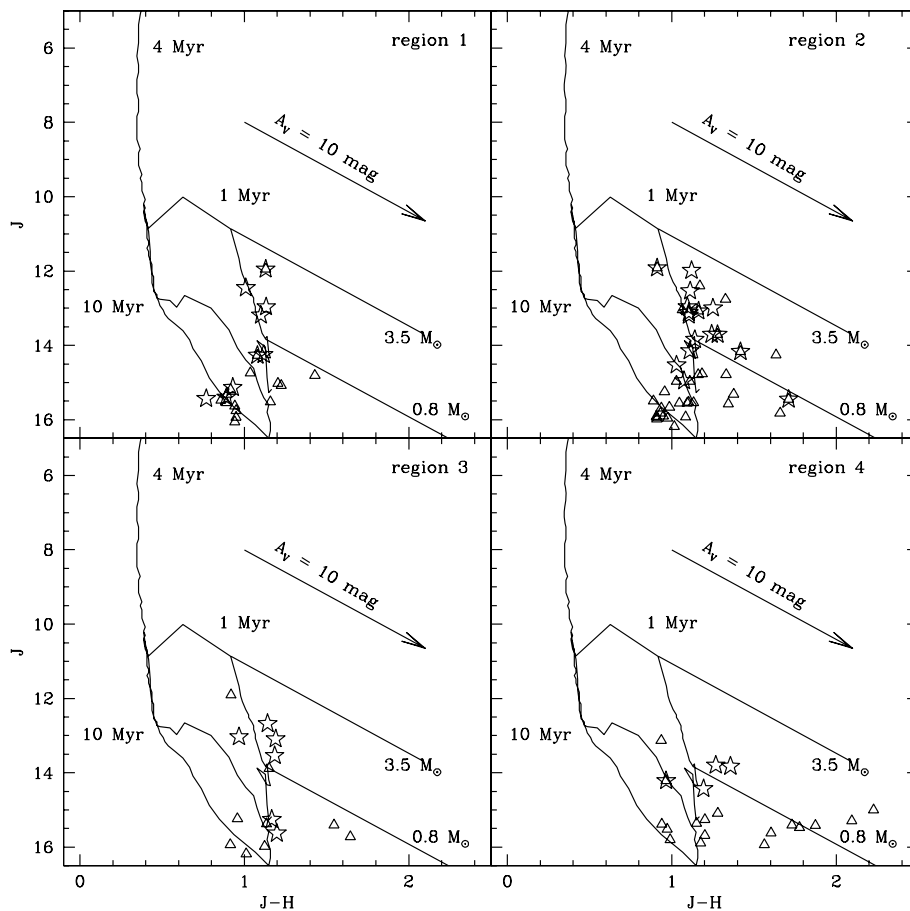
reddening vector (for details see Ogura et al. 2007). Probable MS stars are dereddened individually as described in Section 4.3. The YSOs in the cluster Be 59 (regions 2 and 3) have ages <1 to 2 Myr, whereas all the YSOs except one in Region 1 have ages <1 Myr. Because of high extinction in Region 4, we could not get a sufficient number of  $V$  and  $I$  observations of  $H\alpha$  and NIR excess stars. The majority of probable PMS stars (from statistically cleaned CMD; see Section 4.3) in the cluster region have ages between 1 and 5 Myr. The average age of the massive stars in the cluster region is estimated to be  $\sim 2$  Myr. The presence of significant number (7/12) of YSOs in the central region (Region 2) of the cluster with ages <1 Myr indicates a multi-epoch star formation in the cluster.

Fig. 24 shows  $J$ ,  $(J - H)$  CMDs of the stars in four sub-regions having NIR excess and  $H\alpha$  emission. The isochrones for 4 Myr by Bertelli et al. (1994) and PMS isochrones for 1 and 10 Myr by Siess et al. (2000) are also plotted for  $E(B - V) = 1.4$  mag and distance of 1.0 kpc. Since stars in the field region have  $(J - H) < 1.05$  (cf. Fig. 11b), the stars in the sub-regions having  $(J - H) > 1.05$  are considered as probable members of the Be 59 star-forming region. The CMDs show that Region 4 has more NIR excess stars in comparison to the cluster (regions 2 and 3) supporting the youth of the region. The mass of the probable YSO candidates can be estimated by comparing their locations on the CMD with the evolutionary models of PMS stars. The continuous oblique reddening lines denote the positions of PMS stars (age  $\sim 1$  Myr) of 3.5 and 0.8  $M_{\odot}$ , respectively. The YSOs in all the four sub-regions have masses in the range  $\sim 3.0$ –0.8  $M_{\odot}$ . A comparison of the distribution of stars in Fig. 24 indicates that the Region 2 (central region of Be 59) has relatively more massive stars (of 24 stars, six have masses  $> 2.0 M_{\odot}$ ) in comparison to Region 4 (one star out of 15 stars has mass  $> 2.0 M_{\odot}$ ).

Assuming the number density of the molecular gas and temperature of ionized gas as  $3.5 \times 10^2 \text{ cm}^{-3}$  and  $\sim 10^4$  K, respectively,



**Figure 23.**  $V_0/(V-I)_0$  CMD for probable YSOs lying in three selected regions. The isochrone for 4 Myr age by Bertelli et al. (1994) and PMS isochrones of 1, 2, 5, 10 Myr by Siess et al. (2000) are also shown. All the isochrones are corrected for a distance of 1 kpc. The filled circles, triangles and star symbols represent MS, NIR excess and  $H\alpha$  emission stars, respectively.



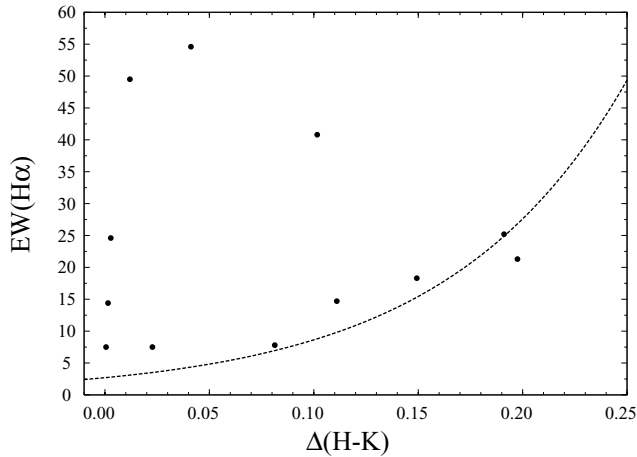
**Figure 24.**  $J, (J-H)$  CMD for probable YSOs lying in four selected regions. The symbols are the same as in Fig. 11. The isochrone of 4 Myr ( $Z = 0.02$ ) by Bertelli et al. (1994) and PMS isochrones of age 1 and 10 Myr by Siess et al. (2000) corrected for a distance of 1 kpc and reddening  $E(B-V)_{\min} = 1.4$  mag are also shown. The continuous oblique lines denote the reddening vectors for PMS stars of  $0.8$  and  $3.5 M_{\odot}$ . The straight line indicates reddening vector for  $A_V = 10$  mag.

Yang & Fukui (1992) have estimated the shock velocity as  $\sim 3 \text{ km s}^{-1}$ . Since the projected distance of clumps C1 and C2 from the cluster centre is  $\sim 3$  pc, the triggering shock would take  $\sim 1$  Myr to reach the clumps. This indicates that the age difference between the PMS stars towards the clumps and triggering stars in the cluster centre should be  $\sim 1-2$  Myr. The age of young clusters is usually derived by fitting the post-MS evolutionary tracks to the earliest members if significant evolution has occurred or by fitting the the-

oretical PMS isochrones to the low-mass contracting population. The  $(J-H)/(H-K)$  colour-colour diagrams (Fig. 22), CMDs (Fig. 24) and distribution of YSOs towards the clumps (Table 5) indicate that the YSOs around the clumps are young (age  $\lesssim 1$  Myr) as compared to those in the cluster. The probable PMS stars in the cluster region show an age spread of  $\lesssim 1-5$  Myr (Fig. 9), whereas NIR excess stars and  $H\alpha$  emission stars have age  $\lesssim 1-2$  Myr. The average post-MS ages of massive stars are estimated as  $\lesssim 2$  Myr.

**Table 6.** Statistics of PMS stars (having  $M_V \sim 0 - 5$  mag), NIR excess and  $H\alpha$  stars in clusters Be 59 and NGC 1893.

Population	Be 59		NGC 1893	
	$r < 5$ arcmin	$5 < r < 10$ arcmin	$r < 3$ arcmin	$3 < r < 6$ arcmin
PMS stars	186	219	99	167
NIR excess stars	11	15	3	10
Percentage of PMS stars having NIR excess	5.9	6.8	3.0	6.0
$H\alpha$ stars	6	8	5	4
Percentage of PMS stars having $H\alpha$ emission	3.2	3.7	5.0	2.4

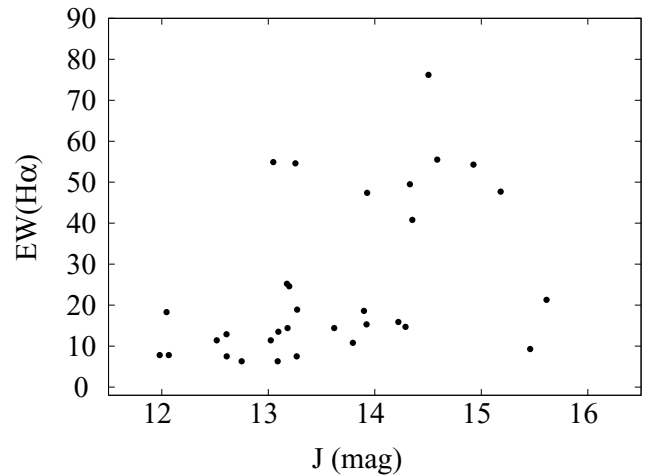
**Figure 25.**  $H\alpha$  equivalent width,  $EW(H\alpha)$ , in  $\text{\AA}$  versus NIR-excess ( $\Delta(H-K)$ ) diagram. The dash curve represents eye-estimated lower profile for the data points shown in fig. 10 of Herbig & Dahm (2002).

Here, it is worthwhile to mention that massive stars are not significantly evolved, therefore age determination of post-age MS stars may be less accurate in comparison to the PMS stars. On the basis of above discussions, the expected age difference between the cluster population and YSOs towards clumps is estimated to be  $\sim 1-2$  Myr. This seems to support the triggered star formation activity towards the clumps due to massive stars in the cluster region.

## 6 THE NIR EXCESS AND $H\alpha$ EMISSION STARS: STATISTICS

To study the effect of environment on the disc around the YSOs, we present statistics of NIR excess stars and  $H\alpha$  emission stars of the clusters Be 59 and NGC 1893 in Table 6. The data for NGC 1893 have been taken from Sharma et al. (2007b). The number of PMS stars in the range  $M_V \sim 0-5$  mag has been estimated from the statistically cleaned CMD as discussed in Section 4.3. The statistics indicate that the inner region of the cluster NGC 1893 shows a less percentage of PMS-NIR excess stars as compared to the outer region, whereas both inner and outer regions of Be 59 show rather a similar distribution of PMS-NIR excess stars. In the case of Be 59, the percentage of PMS-NIR excess stars in the inner region is higher than in the case of NGC 1893.

Strong  $H\alpha$  emission in TTSs generally has been attributed to accretion process, whereas weak emission is believed to arise from chromospheric activity. The TTSs in the young cluster IC 5146 show that NIR excess and equivalent width,  $EW(H\alpha)$ , are well correlated (Herbig & Dahm 2002; Dahm 2005). In Fig. 25, we plot

**Figure 26.**  $H\alpha$  equivalent width,  $EW(H\alpha)$ , in  $\text{\AA}$  as a function of  $J$  mag.

$EW(H\alpha)$  against NIR excess  $\Delta(H-K)$ , defined as the horizontal displacement from the reddening vector at the boundary of ‘F’ and ‘T’ regions (see Fig. 11). Apparently, there does not seem any trend as statistics are poor, however lower profile of the distribution seems to follow the dashed line which is an eye-estimated lower profile for the data points shown in fig. 10 of Herbig & Dahm (2002). Here, we have applied a correction of  $-0.25$  to the  $\Delta(H-K)$  values of Herbig & Dahm (2002) as they measured  $\Delta(H-K)$  from the leftward reddening vector of ‘F’ region.

Fig. 26 shows a plot of  $EW(H\alpha)$  as a function of  $J$  magnitude, which indicates that faint  $H\alpha$  stars ( $J > 14$ , mass  $\lesssim 0.8 M_\odot$ ) have higher  $EW(H\alpha)$  than the brighter stars (mass  $\sim 1-3 M_\odot$ ). This effect may partly be due to magnitude dependence of  $EW(H\alpha)$ , however it appears accretion activity among low-mass members of Be 59 has not subsided. About 32 and 62 per cent of  $H\alpha$  stars of Be 59 and NGC 1893, respectively, show NIR excess in  $(H-K)$  colour (see Table 7). For comparison, this ratio is 66 per cent in IC 5146 (TTSs age  $< 0.7$  Myr), 27 per cent in NGC 2264 (TTSs age  $\sim 1.1$  Myr) and 4 per cent in NGC 2362 (TTSs age  $\sim 1.4$  Myr) (Dahm 2005). The presence of  $H\alpha$  emission and NIR excess in TTS population indicates that the inner disc regions of low-mass stars are still not dissipated.

Table 8 gives the statistics of the YSOs as a function of age. We selected a sample of probable PMS stars in the range  $M_V \sim 0-5$  mag from the statistically cleaned CMDs (cf. Section 4.3). The percentage of NIR excess and  $H\alpha$  emission stars decreases with age. In the cluster Be 59,  $\sim 29$  and 71 per cent of the PMS stars (having age  $\leq 1$  Myr) show NIR excess and  $H\alpha$  excess emission, respectively,

**Table 7.** Statistics of H $\alpha$  stars showing NIR excess in clusters Be 59 and NGC 1893. This table lists all the H $\alpha$  stars which have  $JHK_s$  data.

Population	Be 59		NGC 1893	
	$r < 5$ arcmin	$5 < r < 10$ arcmin	$r < 3$ arcmin	$3 < r < 6$ arcmin
H $\alpha$ stars (having $JHK_s$ data)	12	10	7	9
H $\alpha$ star having NIR excess	4	3	4	6
Percentage of H $\alpha$ stars with NIR excess	33	30	57	67
Density of H $\alpha$ stars (stars/pc <sup>2</sup> )	2.3	0.6	0.4	0.2

**Table 8.** Statistics of YSOs (having  $M_V \sim 0-5$  mag) in clusters Be 59 and NGC 1893. Numbers given in parentheses are in percentage of PMS stars.

Age range (Myr)	Be 59			NGC 1893		
	PMS stars	NIR excess stars	H $\alpha$ stars	PMS stars	NIR excess stars	H $\alpha$ stars
<1	14	4(29)	10(71)	50	5(10)	6(12)
1–2	8	1(13)	2(25)	60	3(5)	2(3)
2–5	22	2(9)	1(5)	49	0(-)	1(2)
5–10	13	1(8)	1(8)	7	0(-)	1(14)

whereas in the case of NGC 1893 this fraction is smaller (10 and 12 per cent, respectively).

Finally, we compare the surface densities of H $\alpha$  emitters in various young star clusters. The slitless spectroscopy of Be 59 and NGC 1893 (Sharma et al. 2007b) is expected to be complete up to  $M_V = 5$ . The surface densities of H $\alpha$  emitters in clusters Be 59 (area  $\simeq 26.6$  pc<sup>2</sup>) and NGC 1893 (area  $\simeq 101$  pc<sup>2</sup>) are found to be 1.0 and 0.2 star pc<sup>-2</sup>, respectively. The surface densities of H $\alpha$  emitters in young clusters NGC 2264 (area  $\simeq 52$  pc<sup>2</sup>) and NGC 2362 (area  $\simeq 22.4$  pc<sup>2</sup>), estimated for magnitude limit  $M_V = 5$  from Dahm (2005), are 1.4 and 0.2 star pc<sup>-2</sup>, respectively. The density of H $\alpha$  emission stars in central region of both the clusters Be 59 and NGC 1893 is higher as compared to the outer region of the clusters (see Table 7).

## 7 SUMMARY

The star formation scenario around young star cluster Be 59 is studied using the optical  $UBVI_c$  photometric data, slitless spectroscopy along with archival data from the surveys such as 2MASS, MSX, IRAS and NVSS. The post-main-sequence age and distance of the cluster are found to be  $\sim 2$  Myr and  $1.00 \pm 0.05$  kpc, respectively. YSOs in the Be 59 region have been identified using NIR TCD and H $\alpha$  emission stars. Following are the main results.

(1) The interstellar extinction in the cluster region is found to be variable with  $E(B - V)_{\min} \simeq 1.4$  mag,  $E(B - V)_{\max} \simeq 1.8$  mag. The ratio of total-to-selective extinction in the cluster region,  $R_{\text{cluster}}$ , is estimated as  $3.7 \pm 0.3$  which indicates an anomalous reddening law consequently a larger grain size in the Be 59 region.

(2) The cluster Be 59 contains OB stars having mean age  $\sim 2$  Myr along with probable PMS stars having age 1–5 Myr. A slitless spectroscopic survey of Be 59 region identifies 48 H $\alpha$  emission stars. The ages of the YSOs (H $\alpha$  emission stars and NIR excess stars) are found to be in the range of  $< 1$  to 2 Myr.

(3) The slope of the IMF ‘ $\Gamma$ ’ in the mass range  $2.5 < M/M_{\odot} \leq 28$  is found to be  $-1.01 \pm 0.11$  which is shallower than the Salpeter

value ( $-1.35$ ), whereas in the mass range  $1.5 < M/M_{\odot} \leq 2.5$  the slope is almost flat. The slope of the KLF is estimated as  $0.27 \pm 0.02$ , which is smaller than the average value ( $\sim 0.4$ ) reported for young clusters.

(4) Approximately 32 per cent of H $\alpha$  emission stars of Be 59 exhibit NIR excess indicating that their inner disc has not yet dissipated. The inner region of the cluster NGC 1893 has smaller percentage of PMS-NIR excess stars as compared to outer region. In the case of Be 59, the percentage of PMS-NIR excess stars in the inner as well as in the outer region is the same.

(5) The  $(J - H)/(H - K)$  colour–colour diagrams and  $J$ ,  $(J - H)$  CMD for the stars lying towards the molecular clumps C1 and C2 (cf. Yang & Fukui 1992) indicate that these stars have higher extinction and relatively larger NIR excess suggesting that they may be younger than the stars in the cluster region. If this is true, then star formation towards the clump regions might be triggered by OB stars in the cluster region.

(6) The surface densities of H $\alpha$  stars, having  $M_V \leq 5$ , for clusters Be 59 and NGC 1893 are found to be 1.0 and 0.2 star pc<sup>-2</sup> which are comparable to the surface densities (for the same magnitude limit) for young clusters NGC 2264 (1.4 star pc<sup>-2</sup>) and NGC 2362 (0.2 star pc<sup>-2</sup>) estimated from Dahm (2005).

## ACKNOWLEDGMENTS

Authors are thankful to the anonymous referee for useful comments. The observations reported in this paper were obtained using the Kiso Schmidt (Japan) and 2-m *HCT* at IAO, Hanle, the high-altitude station of Indian Institute of Astrophysics, Bangalore. We are also thankful to the Kiso Observatory and IAO for allotting observing time. We thank the staff at Kiso (Japan) and IAO, Hanle/its remote control station at CREST, Hosakote for their assistance during the observations. This publication makes use of data from the 2MASS, which is a joint project of the University of Massachusetts and the Infrared Processing and Analysis Centre/California Institute

of Technology, funded by the National Aeronautics and Space Administration and the National Science Foundation. AKP is thankful to the National Central University, Taiwan, and TIFR, Mumbai, for the financial support during his visit to NCU and TIFR, respectively. AKP and KO acknowledge the support given by DST (India) and JSPS (Japan) to carry out the wide field CCD photometry around open clusters. We thank Annie Robin for letting us use her model of stellar population synthesis.

## REFERENCES

- Aumann H. H., Fowler J. W., Melnyk M., 1990, *AJ*, 99, 1674  
 Bertelli G., Bressan A., Chiosi C., Fagotto F., Nasi E., 1994, *A&AS*, 106, 275  
 Bertout C., Basri G., Bouvier J., 1988, *ApJ*, 330, 350  
 Bessell M. S., Brett J. M., 1988, *PASP*, 100, 1134  
 Brandl B., Brandner W., Eisenhauer F., 1999, *A&A*, 352, L69  
 Chen H., Tafalla M., Greene T. P., 1997, *ApJ*, 475, 163  
 Chen W. P., Chen C. W., Shu C. G., 2004, *AJ*, 128, 2306  
 Chini R., Krügel E., 1983, *A&A*, 117, 287  
 Chini R., Wargau W. F., 1990, *A&A*, 227, 5  
 Cohen J. G., Frogel J. A., Persson S. E., Elias J. H., 1981, *ApJ*, 249, 481  
 Dahm S. E., 2005, *AJ*, 130, 1805  
 Dolan C. J., Mathieu R. D., 2002, *AJ*, 123, 387  
 Elmegreen B. G., 1989, *ApJ*, 340, 786  
 Elmegreen B. G., 1998, in Woodward C. E., Shull J. M., Thronson H. A., eds *ASP Conf. Ser. 148, Origins. Astron. Soc. Pac., San Francisco*, p. 150  
 Elmegreen B. G., Lada C. J., 1977, *ApJ*, 214, 725  
 Felli M., Tofani G., Fanti C., Tomasi P., 1977, *A&AS*, 27, 181  
 Ghosh S. K., Ojha D. K., 2002, *A&A*, 388, 326  
 Ghosh S. K., Verma R. P., Rengarajan T. N., Das B., Saraiya H. T., 1993, *ApJS*, 86, 401  
 Harten R. H., Goss W. M., Matthews H. E., Israel F. P., 1981, *A&A*, 103, 50  
 Herbig G. H., 1962, *Adv. Astron. Astrophys.* 1, 47  
 Herbig G. H., 1998, *ApJ*, 497, 736  
 Herbig G. H., Dahm S. E., 2002, *AJ*, 123, 304  
 Hester et al., 1996, *AJ*, 111, 2349  
 Hillenbrand L. A., 1997, *AJ*, 113, 1733  
 Hillenbrand L. A., Strom S. E., Vrba F. J., Keene J., 1992, *ApJ*, 397, 613  
 Johnson H. L., Morgan W. W., 1953, *ApJ*, 117, 313  
 Kaluzny J., Udalski A., 1992, *Acta Astronomica*, 42, 29  
 Kroupa P., 2002, *Sci*, 295, 82  
 Lada E. A., Lada C. J., 1995, *AJ*, 109, 1682  
 Lada E. A., Evans N. J., II, Depoy D. L., Gatley I., 1991, *ApJ*, 371, 171  
 Lada C. J., Lada E. A., 2003, *ARA&A*, 41, 57  
 Lada C. J., Young E. T., Greene T. P., 1993, *ApJ*, 408, 471  
 Landolt A. U., 1992, *AJ*, 104, 340  
 Lee H. T., Chen W. P., Zhang Z. W., Hu J. Y., 2005, *ApJ*, 624, 808  
 Leistra A., Cotera A. S., Leibert J., Burton M., 2005, *AJ*, 130, 1719  
 MacConnell D. J., 1968, *ApJS*, 16, 275  
 Massey P., Johnson K. E., Eastwood K. D., 1995, *ApJ*, 454, 151  
 Megeath S. T., Herter T., Beichmann C., Gautier N., Hester J. J., Rayner J., Shupe D., 1996, *A&A*, 307, 775  
 Mermilliod J. C., 1995, in Egret D., Albrecht M. A., eds, *Information and Online Data in Astronomy*. Kluwer Academic Press, Dordrecht, p. 127  
 Meyer M., Calvet N., Hillenbrand L. A., 1997, *AJ*, 114, 288  
 Morgan L. K., Thompson M. A., Urquhart J. S., White G. J., Miao J., 2004, *A&A*, 426, 535  
 Morgan L. K., Thompson M. A., Urquhart J. S., White G. J., Miao J., 2006, *A&A*, 457, 207  
 Ogura K., Sugitani K., Pickles A., 2002, *AJ*, 123, 2597  
 Ogura K., Chauhan N., Pandey A. K., Bhatt B. C., Ojha D., Itoh Y., 2007, *PASJ*, 59, 199  
 Ojha D. K. et al., 2004a, *ApJ*, 608, 797  
 Ojha D. K. et al., 2004b, *ApJ*, 616, 1042  
 Okada Y., Onaka T., Shibai H., Doi Y., 2003, *A&A*, 412, 1990  
 Pandey A. K., Ogura K., Sekiguchi K., 2000, *PASJ*, 52, 847  
 Pandey A. K., Nilakshi, Ogusa K., Sagar R., Tarusawa K., 2001, *A&A*, 374, 504  
 Pandey A. K., Upadhyay K., Nakada Y., Ogura K., 2003, *A&A*, 397, 191  
 Pandey A. K., Upadhyay K., Ogura K., Sagar R., Mohan V., Mito H., Bhatt H. C., Bhatt B. C., 2005, *MNRAS*, 358, 1290  
 Preibisch T., Zinnecker H., 1999, *AJ*, 117, 2381  
 Price S. D., Egan M. P., Carey S. J., Mizuno D. R., Kuchar T. A., 2001, *AJ*, 121, 2819  
 Robin A. C., Reyle C., Derriere S., Picaud S., 2003, *A&A*, 409, 523  
 Robitaille T. P., Whitney B. A., Indebetouw R., Wood K., Denzmore P., 2006, *ApJS*, 167, 256  
 Rossano G. S., Russell R. W., Cornett R. H., 1980, *PASP*, 92, 357  
 Salpeter E. E., 1955, *ApJ*, 121, 161  
 Sanchawala K. et al., 2007, *ApJ*, 667, 963  
 Sharma S., Pandey A. K., Ogura K., Mito H., Tarusawa K., Sagar R., 2006, *AJ*, 132, 1669  
 Sharma S., Ogura K., Pandey A. K., Ojha D. K., Bhatt B. C., 2007a, *Bull. Astron. Soc. India*, 35, 53  
 Sharma S., Pandey A. K., Ojha D. K., Chen W. P., Ghosh S. K., Bhatt B. C., Maheswar G., Sagar R., 2007b, *MNRAS*, 380, 1141  
 Schmidt-Kaler Th., 1982, in Schaifers K., Voigt H. H., Landolt H., eds, *Landolt-Bornstein*, Vol. 2b. Springer, Berlin, p. 19  
 Siess L., Dufour E., Forestini M., 2000, *A&A*, 358, 593  
 Stetson P. B., 1987, *PASP*, 99, 191  
 Stetson P. B., 1992, in Warrall D. M., Biemesderfer C., Barnes J., eds, *ASP Conf. Ser. Vol. 25, Astronomical Data Analysis Software and System I*. Astron. Soc. Pac., San Francisco, p. 297  
 Sugitani K., Fukui Y., Ogura K., 1991, *ApJS*, 77, 59  
 Yang J., Fukui Y., 1992, *ApJ*, 386, 618

## SUPPLEMENTARY MATERIAL

The following supplementary material is available for this article:

**Table 2.**  $UBVI_c$  photometric data of the stars in the field of Be 59.  $X, Y$  are the pixel coordinates. Radius is with respect to the centre  $X = 1128, Y = 1024$  ( $\alpha_{2000} = 00^{\text{h}}02^{\text{m}}10^{\text{s}}.4, \delta_{2000} = 67^{\circ}25'10''$ ). One pixel corresponds to 1.5 arcsec.

This material is available as part of the online article from: <http://www.blackwell-synergy.com/doi/abs/10.1111/j.1365-2966.2007.12641.x>  
 (this link will take you to the article abstract).

Please note: Blackwell Publishing are not responsible for the content or functionality of any supplementary materials supplied by the authors. Any queries (other than missing material) should be directed to the corresponding author for the article.

This paper has been typeset from a  $\text{T}_{\text{E}}\text{X}/\text{L}_{\text{A}}\text{T}_{\text{E}}\text{X}$  file prepared by the author.